In: Trends in Polyoxometalates Research ISBN: 978-1-63482-656-3
Editors: Laurent Ruhlmann and Delphine Schaming

Chapter 6

POLYOXOMETALATE-BASED SINGLE-MOLECULE MAGNETS

***Natalya V. Izarova*[*1] *and Paul Kögerler*[†1,2]**
[1]Peter Grünberg Institute – PGI 6, Forschungszentrum Jülich, Jülich, Germany
[2]Institute of Inorganic Chemistry, RWTH Aachen University, Aachen, Germany

ABSTRACT

Contrasting the rapid development of single-molecule magnets (SMMs) based on classical polynuclear transition metal coordination complexes since the early 1990s, magnetically functionalized polyoxometalates exhibiting SMM characteristics were identified for the first time only in 2008. This chapter details the development of this class of POMs with a particular focus on spin structures based on first-row transition metal ions. We also illustrate the specific challenges and issues when designing and synthesizing polyoxometalate-based SMMs.

Keywords: single-molecule magnets, magnetism

ABBREVIATIONS

POM	polyoxometalate
POT	polyoxotungstate
POMo	polyoxomolybdate
SMM	single-molecule magnet
QTM	quantum tunneling of the magnetization
DC field	direct current (static) field
AC field	alternating current (oscillating) field

[*] Email: n.izarova@fz-juelich.de.
[†] Email: paul.koegerler@ac.rwth-aachen.de.

1. INTRODUCTION

The term "single-molecule magnet" was coined nearly a quarter-century ago and commonly refers to a molecular compound that, at sufficiently low temperatures, exhibits slow magnetic relaxation. This includes features which become evident below a compound-specific blocking temperature such as hysteresis of the field-dependent magnetization, akin to typical solid-state ferro- and ferrimagnets [1]. These characteristics are purely of molecular origin and require no long-range cooperative magnetic ordering. They are typically related to the combination of a high-spin ground state and significant molecular magnetic anisotropy. In a simple model description temperature-dependent slowing of the magnetization dynamics, which is observable in the frequency dependence and the emergence of out-of-phase components in the *ac* magnetic susceptibility data, is related to the molecular ground state properties. Of particular importance here is the lifting of the 2*S*+1-fold degeneracy of the ground state multiplet characterized by a total spin quantum number *S* due to spin-orbit coupling and ligand field effects. This so-called zero-field splitting (ZFS) results in different energies for the m_S substates (ranging from $m_S = +S, +S–1, \ldots$ to $–S$).

Typically, the discussion and interpretation of these key SMM features are limited to an "effective spin" model [2]. Prior to the emergence of SMM as a seminal topic in molecular magnetism in the early 1990s, this model has been developed and used for electron spin resonance experiments where the focus is on the ground state multiplet of a compound [3]. The model is historically motivated by the observation that certain first-row transition metal ions are typically found in ligand field environments with local symmetries that effectively quench the orbital momentum of the magnetically relevant valence electrons. Therefore, their magnetic behavior is comparable to a pure spin center. This spin is called effective or pseudo-spin $\tilde{\boldsymbol{S}}$ since it usually differs from the true spin [4]. A weak octahedral ligand field splits the Russell-Saunders terms of a d^n ion into *E*, T_2 (d^1, d^6, d^4, d^9), A_2, T_2, T_1 (d^3, d^8, d^2, d^7), and A_1 terms (d^0, d^5, d^{10}). Only d^3, d^5 and d^8 ions that are characterized by an energetically well-isolated *A* ground state term may be described as pure spin systems in such a coordination environment. In case of d^3 and d^8 ions (A_2) the electron spin Landé *g*-factor ($g_e = 2.00232$) has to be changed to $g_{eff} \neq g_e$.

With decreasing ligand-field symmetry the effective spin Hamiltonian has to be expanded to provide an adequate quantitative description of the system's magnetic observables. An effective Hamiltonian is commonly written as a power series in $\tilde{\boldsymbol{S}}$ and further phenomenological operators account for *e. g.* effective Zeeman splitting or effective spin-orbit coupling like $\tilde{\boldsymbol{L}}\cdot\tilde{\boldsymbol{S}}$ (when Russell-Saunders coupling is adequate). In the context of the discussion of SMMs in the literature, the effective spin Hamiltonian usually is defined in the second-order ZFS approximation:

$$\hat{H}_{\mathrm{eff}} = \underbrace{D\left[\hat{\tilde{S}}_z^2 - \frac{1}{3}\hat{\tilde{\boldsymbol{S}}}^2\right] + E\left(\hat{\tilde{S}}_x^2 - \hat{\tilde{S}}_y^2\right)}_{ligand\ field} + \underbrace{\mu_{\mathrm{B}}\boldsymbol{B}\cdot\boldsymbol{g}\cdot\hat{\tilde{\boldsymbol{S}}}}_{Zeeman}$$

Here, the ligand field component contains two purely empirical energy parameters D and E. For easy axis-type anisotropy of the molecular magnetization, E is assumed to be vanishingly small. In this case – applicable to numerous prototypal SMMs – the eigenvalues of $m_{\tilde{S}}$ substates belonging to the effective ground state quantum number $\tilde{S}$, plotted *versus* the $m_{\tilde{S}}$ values, form a parabola. For negative D values, this establishes an arrangement between the $m_{\tilde{S}} = \pm\tilde{S}$ states that defines an energy barrier for thermally induced changes to the magnetization, such as in response to variation of an external magnetic field. At low temperatures the thermal energy k_BT becomes small compared to the barrier height $|D|\tilde{S}^2$ (or $|D|(\tilde{S}^2 - 1/4)$ for half-integer $\tilde{S}$ values), and the system becomes trapped in one of the energetically lowest $m_{\tilde{S}} = \pm\tilde{S}$ states. The thermal reorganization of the molecular magnetization then often approximates a simple Arrhenius equation ($\tau = \tau_0 \cdot \exp[U_{\text{eff}}/(k_B T)]$, τ relaxation time, τ_0 time constant or pre-exponential factor, U_{eff} effective energy barrier, T temperature). However, several alternative relaxation mechanisms exist in addition to that of thermally induced relaxation that has to "climb the $|D|\tilde{S}^2$ barrier". For example, the temperature-independent phenomenon of quantum tunneling between energetically degenerate $m_{\tilde{S}}$ states (the so-called tunneling of the Neél vector or quantum tunneling of the magnetization, QTM) provides additional relaxation pathways. This leads to a decrease of the effective blocking temperature (sometimes by several orders of magnitude), below which hysteresis of the molecular magnetization is evident, compared to what could be expected from the barrier height $|D|\tilde{S}^2$. Sometimes, such quantum tunneling-based relaxation can be suppressed by a small external magnetic field that, via the Zeeman effect, causes the $\pm m_{\tilde{S}}$ states not to be in resonance anymore. For this reason the *ac* susceptibility of SMMs is often reported in the presence of an applied small static bias field. Several aspects, such as the presence of stray fields and dipole-dipole interactions, all affect these relaxation characteristics, therefore it remains difficult to predict and interpret the relative roles of these various relaxation mechanisms. From a magnetochemical point of view, the interpretation of the magnetic characteristics of the vast majority of POM-based SMMs generally follows the corresponding interpretation of conventional SMMs based on polynuclear coordination complexes. In order to avoid confusion with the practice in the literature where usually effective models are employed, we will in the following not distinguish between the effective spin quantum number $\tilde{S}$ and the spin quantum number S.

The aim of this chapter is to give a representative overview of first-row transition metal-functionalized polyoxometalates (POMs) exhibiting SMM behavior.

Unlike the class of SMM materials based on polynuclear magnetic coordination complexes stabilized by organic ligands, the area of POM-SMMs started to actively develop only over the past seven years. Nevertheless, the accumulated progress in this direction already allows us to distinguish some prospective synthetic pathways and strategies which could potentially lead to compounds with magnetic characteristics and properties interesting for applications of POM-SMMs in, *e. g.*, molecular spintronics [5]. We intentionally limit the scope of this chapter to first-row transition metal-based polyanions as their magnetic behavior can often be described using the afore-mentioned effective spin model. A brief overview on the lanthanide-based polyanions that show slow relaxation of magnetization associated with spin-orbit coupling-based magnetic anisotropy (so-called single-ion magnets) is available in the recent review of Clemente-Juan, Coronado and Gaita-Ariño [6] and the latest publications of the Coronado group [7-8].

The currently existing POM-SMM compounds comprising 3*d* transition metal spin clusters can be divided into two major groups: (1) genuine POM-SMMs where the polyanions incorporate magnetic cores into their (otherwise diamagnetic) framework structures, and (2) a number of compounds where POMs are not SMMs but are only employed for spatial separation of the positively charged magnetic complexes in their crystal lattices to minimize intermolecular magnetic coupling, *i. e.* for magnetic dilution purposes.

2. SINGLE-MOLECULE MAGNETS BASED ON MULTINUCLEAR TRANSITION METAL MAGNETIC CORES AND POLYOXOTUNGSTATE OR POLYOXOMOLYBDATE LIGANDS

Lacunary (or vacant) polyoxotungstates (POTs) and -molybdates (POMos), which can be derived from so-called "plenary" polyanions of the Keggin, $[XM_{12}O_{40}]^{n-}$, or Wells-Dawson, $[X_2M_{18}O_{61}]^{n-}$, structure archetypes (M = W, Mo) by removal of one or more W^{VI} or Mo^{VI} centers (synthetically achievable at defined reaction conditions), are well known for their capacity to serve as multidentate all-inorganic ligands. To date, an impressive variety of POTs and POMos complexes with transition metals, main group elements and lanthanides, spanning a wide range of compositions, nuclearities and structures are known. In the context of this chapter, lacunary POMs have been successfully used to stabilize polynuclear assemblies of magnetic metal ions with the nuclearity ranging from four to sixteen within an inorganic metal-oxide framework. As polydentate ligands possessing vacant sites with rigid geometries, such species have been shown to direct assemblies of polynuclear magnetic cores with desirable topologies.

In addition, nanosized POTs and POMos can also efficiently isolate the magnetic cores from each other, preventing or at least significantly reducing intermolecular interactions. Furthermore, most POTs are thermally stable and robust toward redox treatment, key properties which render POM-SMMs attractive candidates for creating spintronic devices.

2.1. POM-SMMs Prepared by Reacting POTs with Polynuclear Magnetic Coordination Clusters As a Source of High-Valent Mn Ions

One of the approaches to the incorporation of magnetic cores into POM frameworks is based on a metathesis of organic groups in preformed polynuclear magnetic species with POT units [9-10]. This synthetic strategy has been successfully applied to create POM complexes showing slow relaxation of magnetization.

A significant amount of the efforts performed in this direction to date has exploited the famous $[Mn^{IV}_4Mn^{III}_8O_{12}(CH_3COO)_{16}(H_2O)_4]\cdot 4H_2O\cdot 2CH_3COOH$ (Mn_{12}-OAc) complex, a prototypal SMM with a high-spin (S = 10) ground state, as a precursor susceptible to hydrolysis for reactions with POTs. Although it has been impossible until now to retain the $\{Mn^{IV}_4Mn^{III}_8O_{12}\}$ core and directly attach it to robust inorganic POM ligands, it was shown that the slow decomposition of the Mn_{12}-OAc species in aqueous media in the presence of various lacunary POTs can lead to a number of polyanions with fascinating architectures based on high-valent Mn^{III} and Mn^{IV} centers [11-19]. Nevertheless some of the very first

publications on these compounds voiced disappointment as the obtained complexes did not exhibit the expected SMM behavior.

Thus, in 2009 Wang's group reported on a $[\{Mn^{III}_{13}Mn^{II}O_{12}(PO_4)_4\}\{PW_9O_{34}\}_4]^{31-}$ polyanion (abbreviated herein as Mn_{14}-POM) prepared by reacting Mn_{12}-OAc with the trilacunary Keggin-type POT $[B\text{-}\alpha\text{-}PW_9O_{34}]^{8-}$ (B-PW_9) in aqueous medium. The structure of the Mn_{14}-POM could be rationalized in terms of two Mn_4PW_9 and two $Mn^{III}_3PW_9$ structural units connected via oxo bridges and four phosphate groups. The former species, Mn_4PW_9, are composed of cubane-type $\{Mn^{III}_4O_4\}$ or $\{Mn^{III}_3Mn^{II}O_4\}$ clusters grafted onto the vacant site of B-PW_9 while in the latter units the B-PW_9 polyanions are coordinated with three Mn^{III} centers. The *dc* magnetic susceptibility measurements on Mn_{14}-POM indicated strong dominant antiferromagnetic interactions between the manganese centers within the $\{Mn^{III}_{13}Mn^{II}O_{12}(PO_4)_4\}$-core with no possibility to unambiguously determine the ground state spin quantum number from the obtained data. In addition the complex did not exhibit magnetization hysteresis or out-of-phase *ac* susceptibility signals down to 1.8 K. These magnetic features were attributed to a non-typical coordination environment of the Mn^{III} centers in the Mn_{14}-POM, which exhibits five short and one longer Mn–O distances, thus deviating from the typical axial Jahn-Teller distortion of Mn^{III} centers with two elongated *trans*-oriented Mn–L bonds, which is apparently a result of a high rigidity of the POM skeleton directing formation of the Mn_{14} core [11].

A year later Fang, Kögerler and co-workers reported the grafting of the cubane-type $\{Mn^{III}_3Mn^{IV}O_4\}$ cluster onto a vacant site of trilacunary Wells-Dawson tungstophosphate $[\alpha\text{-}P_2W_{15}O_{56}]^{12-}$ (P_2W_{15}) to provide $[(\alpha\text{-}P_2W_{15}O_{56})Mn^{III}_3Mn^{IV}O_3(CH_3COO)_3]^{8-}$ ($Mn_4P_2W_{15}$) polyanions which were prepared by reacting Mn_{12}-OAc with P_2W_{15} in aqueous acetic acid solution. The $\{Mn^{III}_3Mn^{IV}O_3X\}$ (X = halides, NO_3^-, *etc.*) cubane-type assemblies supported by organic ligands constitute a well-known family of SMMs with spin 9/2 ground states and ZFS parameters D ranging from –0.3 to –0.6 cm^{-1} [20]. In the structure of $Mn_4P_2W_{15}$ all three Mn^{III} centers are coordinated by the P_2W_{15} units with the O atom of the central PO_4 group in P_2W_{15} acting as one of the Mn_4O_4 "cubane" vertex and defining the intersection of the Jahn-Teller axes for the Mn^{III} centers. The Mn^{IV} ion forms the apex of the $\{Mn^{III}_3Mn^{IV}\}$ trigonal pyramid and is linked to the Mn^{III} centers by three μ_3-oxo ligands each connecting the Mn^{IV} and two Mn^{III} ions, and μ_2-acetate groups bridging the every Mn^{III}/Mn^{IV} pair (Fig. 1, top left).

Like the known coordination complex-based SMMs with the $\{Mn^{III}_3Mn^{IV}O_3X\}$ core, the $Mn_4P_2W_{15}$ species also possess an S = 9/2 ground state due to antiferromagnetic coupling between the Mn^{IV} (isotropic spin-3/2) and Mn^{III} (anisotropic spin-2) centers ($J_{3\text{-}4}$ = –31.3 cm^{-1}) and ferromagnetic coupling between the Mn^{III} centers ($J_{3\text{-}3}$ = +10.2 cm^{-1}), as deduced from detailed analysis of the *dc* susceptibility data. The shapes of field-dependent magnetization curves at low temperatures (1.8 – 5 K) reflect strong deviations from isotropic pure-spin Brillouin functions, *i. e.* significant magnetic anisotropy, due to ligand field effects associated with the Jahn-Teller-distorted Mn^{III} sites. However, the polyanions surprisingly did not show any out-of-phase χ" signal in the *ac* susceptibility measurements down to 1.8 K and thus did not exhibit slow magnetization relaxation, in a sharp contrast to all previously known $\{Mn^{III}_3Mn^{IV}O_3X\}$-based SMMs. The positive ZFS parameter D = +0.36 cm^{-1} found for $Mn_4P_2W_{15}$ indicates an inversion of the parabola of the zero field-split m_S substates belonging to the ground state resulting in the loss of the thermal relaxation barrier, in stark contrast to all known SMMs with the cubane-like $\{Mn^{III}_3Mn^{IV}O_3X\}$ core [12].

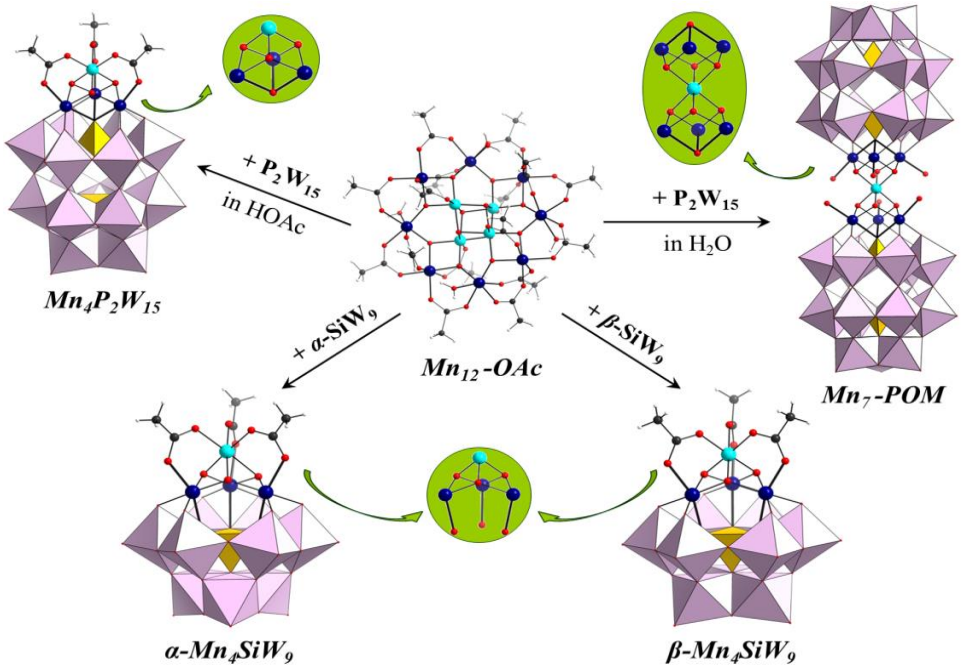

Figure 1. Polyanions incorporating cubane $\{Mn^{III}_3Mn^{IV}O_4\}$ or double-cubane $\{Mn^{III}_6Mn^{IV}O_6(H_2O)_6\}$ magnetic cores prepared starting from the Mn_{12}-OAc precursor (center): $Mn_4P_2W_{15}$ (top left), Mn_7-POM (top right), β-Mn_4SiW_9 in Mn_4SiW_9-I (bottom right) and α-Mn_4SiW_9 in Mn_4SiW_9-II (bottom left). Color legend: WO_6 pink octahedra, XO_4 yellow tetrahedra (X = P, Si); Mn^{IV} cyan, Mn^{III} dark-blue, O red, C black, H white spheres. The corresponding magnetic cores are enlarged and highlighted in the green insets. The elongated Mn–O bonds in the direction of the Jahn-Teller axes of the Mn^{III} centers are highlighted as bold black bonds.

Performing the reaction between the same reagents, Mn_{12}-OAc and P_2W_{15}, in H_2O instead of a diluted acetic acid led to the C_i-symmetric polyanion $[(\alpha\text{-}P_2W_{15}O_{56})_2Mn^{III}_6Mn^{IV}O_6(H_2O)_6]^{14-}$ (Mn_7-POM), where a $\{Mn^{III}_6Mn^{IV}O_6(H_2O)_6\}$ magnetic cluster is sandwiched between the two P_2W_{15} units. The structure of the $\{Mn^{III}_6Mn^{IV}O_6(H_2O)_6\}$ core can be viewed as two $\{Mn^{III}_3Mn^{IV}O_3(H_2O)_3\}$ cubane-like assemblies with a shared Mn^{IV} apex which is also the only isotropic spin center in this cluster (Fig. 1, top right). Additionally, the acetate ligands bridging the Mn^{III} and Mn^{IV} centers in $Mn_4P_2W_{15}$, are replaced by terminal water ligands withing the Mn_7-core of Mn_7-POM. Analysis of the susceptibility data for $Na_{14}[Mn_7\text{-POM}]\cdot 68H_2O$ points to an S = 21/2 ground state arising from antiferromagnetic exchange interactions between the Mn^{III} and Mn^{IV} ions ($J_{3\text{-}4}$ = –18.75 cm^{-1}) and ferromagnetic coupling between the spins of the Mn^{III} centers ($J_{3\text{-}3}$ = +12.5 cm^{-1}). At the same time the Mn^{III}–Mn^{IV} coupling in Mn_7-POM is significantly weaker than that in $Mn_4P_2W_{15}$ indicating an important contribution of acetate super-exchange pathways in the latter compound. The frequency-dependent *ac* susceptibility measurements indicated SMM features with frequency-dependent out-of-phase components visible below 3 K. The empirical ZFS D value of –0.143 cm^{-1} was determined from model calculations using the computational framework CONDON [21]. Unfortunately the determination of the effective energy barrier U_{eff} failed because no maxima in χ'' *vs* T or Cole-Cole (χ'' *vs* χ') plots were observed within the experimental temperature and frequency limits [15].

The difference in the magnetic properties of Mn_7-POM and $Mn_4P_2W_{15}$ polyanions possessing structurally similar magnetic cores might be attributed to the better shielding of the magnetic clusters in the former POM by P_2W_{15} ligands minimizing the possibility for intermolecular interactions. Additionally, the Mn_7-POM does not possess a dipole moment while $Mn_4P_2W_{15}$ does, which may result in different modes of ZFS in these polyanions [15]. Note that nearly all existing POM-SMMs exhibit no or only a small dipole moment, in line with the observations comparing Mn_7-POM and $Mn_4P_2W_{15}$.

The potential role of the efficient separation between the magnetic polyanions in the crystal lattice is further highlighted by studies of trilacunary [*A*-*β*-$SiW_9O_{34}]^{10-}$ Keggin-type POMs that support a similar cubane magnetic assembly, $\{Mn^{III}_3Mn^{IV}O_3(CH_3COO)_3\}$. Unlike in P_2W_{15} or *B*-PW_9 (which constitute the $Mn_4P_2W_{15}$ and the Mn_{14}-POM, respectively) where the central PO_4 tetrahedron is exposed to the vacant site by just one oxygen atom acting as a vertex of the Mn_4O_4 cubane motif (Fig. 1, top left), the inner XO_4 tetrahedron in the *A*-type trilacunary Keggin polyanions [*A*-*β*-$XW_9O_{34}]^{n-}$ ($X = P^V$, Si^{IV}, Ge^{III}, Al^{III} *etc*) is turned to the lacunary site by one of its faces (Fig. 1, bottom). This leads to a coordination mode of the cubane-like tetramanganese core in [(*A*-*β*-SiW_9O_{34})$Mn^{III}_3Mn^{IV}O_3(CH_3COO)_3]^{6-}$ (Mn_4SiW_9) different than that observed in $Mn_4P_2W_{15}$. Thus the three Mn^{III} centers of the $\{Mn^{III}_3Mn^{IV}O_3(CH_3COO)_3\}$ core are each coordinated to three different O atoms of the inner SiO_4 group of the *A*-SiW_9 ligand which results in almost parallel alignment of their Jahn-Teller axes in Mn_4SiW_9 (Fig. 1, bottom right), which is linked to a significant increase of the cluster's total magnetic anisotropy and ZFS.

Initially the Mn_4SiW_9-type POMs were prepared by reacting Mn_{12}-OAc, $[Ce^{IV}Mn^{IV}_6O_9(O_2CCH_3)_9(NO_3)(H_2O)_2]$ and [*A*-*β*-$SiW_9O_{34}H]^{9-}$ in aqueous medium, leading to the isolation of the salt $Na_2[(CH_3)_2NH_2]_{20}$[(*A*-*β*-$SiW_9O_{34})_2Ce^{IV}_4O_2(CH_3COO)_2$][(*A*-*β*-$SiW_9O_{34}$)$Mn^{III}_3Mn^{IV}O_3$-$(CH_3COO)_3]_2 \cdot 58H_2O$ (Mn_4SiW_9-I) where the Mn_4SiW_9 POMs co-crystallize with diamagnetic [(*A*-*β*-$SiW_9O_{34})_2Ce^{IV}_4O_2(CH_3COO)_2]^{10-}$ polyanions [16]. Fitting the *dc* magnetic susceptibility data for this compound yielded the coupling constants $J_{3\text{-}4} = -26.93$ cm^{-1} and $J_{3\text{-}3} = +3.17$ cm^{-1}, with the latter value being about 3 times smaller than the exchange coupling constant $J_{3\text{-}3}$ found for $Mn_4P_2W_{15}$. This observation is consistent with a removal of the super-exchange pathway between the Mn^{III} centers in Mn_4SiW_9 via the shared O atom of the central SiO_4 group. The data also suggest an energetically well-isolated $S = 9/2$ ground state with the first excited state $S = 7/2$ at 118.8 cm^{-1}, in line with numerous previously published $\{Mn^{III}_3Mn^{IV}O_3X\}$-based coordination cluster SMM compounds. Fitting of the field-/temperature-dependent magnetization data resulted in the following parameters for Mn_4SiW_9: $D = -0.86$ cm^{-1}, $E = -0.002$ cm^{-1}, and $g_{iso} = 2.01$, providing an upper limit for the potential energy barrier $U = |D|(S^2 - 1/4)$ of 17.2 cm^{-1}. It should be noted that the magnitude of the axial magnetic anisotropy *D* for Mn_4SiW_9-I is one of the largest reported for the cubane-type $\{Mn^{III}_3Mn^{IV}O_3X\}$ clusters. The *ac* susceptibility measurements confirmed slow magnetization relaxation at low temperatures. The effective energy barrier U_{eff} estimated from $\ln(1/\tau)$ values, obtained from the out-of-phase *ac* χ" data *vs* $1/T$, was 17.7 cm^{-1} with a pre-exponential factor $\tau_0 = 1.5\times10^{-7}$ s. The closeness of the experimental U_{eff} value to the thermodynamic barrier *U* combined with a nearly vanishing transverse anisotropy parameter *E* indicates effective suppression of quantum tunneling-based relaxation in Mn_4SiW_9-I [16].

It is also very interesting to compare the magnetic properties of Mn_4SiW_9 co-crystallized with [(*A*-*β*-$SiW_9O_{34})_2Ce^{IV}_4O_2(CH_3COO)_2]^{10-}$ species in Mn_4SiW_9-I with those for the recently

reported compound $Na_{3.5}K_{2.5}[(A\text{-}\alpha\text{-}SiW_9O_{34})Mn^{III}{}_3Mn^{IV}O_3(CH_3COO)_3]\cdot 20H_2O\cdot CH_3COONa\cdot 0.5CH_3COOK$ (Mn_4SiW_9-II), which contains only $[(A\text{-}\alpha\text{-}SiW_9O_{34})Mn^{III}{}_3Mn^{IV}O_3(CH_3COO)_3]^{6-}$ polyanion [19]. The structure of $[(A\text{-}\alpha\text{-}SiW_9O_{34})Mn^{III}{}_3Mn^{IV}O_3(CH_3COO)_3]^{6-}$ is based on the *alpha* isomer of SiW_9, which differs from the Mn_4SiW_9 containing $[A\text{-}\beta\text{-}SiW_9O_{34}]^{10-}$ POT ligands by rotation of the bottom W_3O_{13} triad by 60° (Fig. 1, bottom left). Nevertheless the structure of the magnetic core and its coordination mode to the POT in both the *alpha* and *beta* isomers of Mn_4SiW_9 is very similar, justifying a direct comparison of the magnetic properties of Mn_4SiW_9-I and Mn_4SiW_9-II. Surprisingly, the magnetic behavior of the substances appeared to be quite different. Thus, the analysis of the *dc* susceptibility data as a function of temperature for Mn_4SiW_9-II suggests predominant population of the three states with S = 5/2 (ground state), S = 7/2 (+0.37 cm^{-1}) and S = 3/2 (+1.05 cm^{-1}) at low temperatures. The calculated exchange energies indicate exclusively antiferromagnetic interactions between the metal centers within the $\{Mn^{III}{}_3Mn^{IV}O_3(CH_3COO)_3\}$ assembly in Mn_4SiW_9-II ($J_{3\text{-}4} = -2.3$ cm^{-1}; $J_{3\text{-}4} = -1.2$ cm^{-1}; $J_{3\text{-}3} = -7.1$ cm^{-1}; $J_{3\text{-}4} = -35.2$ cm^{-1}; g = 2.03). At the same time it should be mentioned that these constants for Mn_4SiW_9-II were determined using the $J_{3\text{-}3}$ coupling constants calculated for the $Mn^{III}{}_3SiW_9$ species reported in the same manuscript and varying only the $J_{3\text{-}4}$ parameters during the calculations process. The *ac* measurements on Mn_4SiW_9-II showed neither frequency-dependence nor out-of-phase signal for the magnetic susceptibility, which was explained by the presence of population redistribution between the energetically close spin states and/or supposedly positive ZFS parameters which could not be reliably defined for this system [19].

The above results highlight the important role of the magnetic dilution in the Mn_4SiW_9-I sample by co-crystallization of the Mn_4SiW_9 polyanions with diamagnetic $[(A\text{-}\beta\text{-}SiW_9O_{34})_2Ce^{IV}{}_4O_2(CH_3COO)_2]^{10-}$ species to prevent intermolecular magnetic exchange and limit the extent of quantum tunneling effects. On the other hand, the different crystal packing of the $[(A\text{-}\alpha/\beta\text{-}SiW_9O_{34})Mn^{III}{}_3Mn^{IV}O_3(CH_3COO)_3]^{6-}$ polyanions in Mn_4SiW_9-I and Mn_4SiW_9-II causes slight variations in bonds length and angles within the $\{Mn^{III}{}_3Mn^{IV}O_3(CH_3COO)_3\}$ magnetic core, which may also explain the difference in the magnetic properties and different ground spin states of the Mn_4SiW_9 species in the both materials. Thus, the Mn^{III}–O distances in Mn_4SiW_9-I (average 1.94 Å for the short distances and 2.19 Å for the elongated bonds) are slightly shorter than those in Mn_4SiW_9-II (1.95 Å and 2.25 Å, respectively) revealing a total elongation of the $\{Mn^{III}{}_3Mn^{IV}O_3(CH_3COO)_3\}$ core in the direction from the Si^{IV} atom of the POT ligand toward the Mn^{IV} center of the magnetic core in Mn_4SiW_9-II [16, 19]. This also indicates the advantage of using of all-inorganic POM ligands for stabilization of the multinuclear magnetic cores in POM-SMMs (as observed in Mn_7-POM and some POMs shown in the section 1.2) to provide more rigidity and better separation for the multinuclear magnetic assemblies, over the cases where the magnetic core is isolated by both POM and organic ligands, like in Mn_4SiW_9.

Generally, it is interesting to note that all the POMs with SMM properties obtained by synthetic strategies that employ pre-formed multi-nuclear magnetic species as precursors are based on manganese centers. This offers room for studies on reactivity of multinuclear clusters of other transition metals or mixed 3d-4f assemblies toward POT which may result in complexes possessing intriguing structures and magnetic properties.

2.2. POM-SMMs Assembled by Condensation of Mononuclear Magnetic Metal Ions Precursors

Another strategy toward the construction of rigid POM frameworks incorporating multinuclear magnetic cores relies on self-assembly reactions undergone by magnetic metal ions in the presence of lacunary POMs. Compared to the first approach utilizing ligand metathesis in the pre-formed multinuclear magnetic clusters, this synthetic strategy allows much less control and limits the prediction of the final product, as the self-assembly process can be affected by numerous synthetic parameters (*e. g.*, reagents ratios, pH, reaction temperature, ionic strength, countercations, *etc.*) along with the vacant site geometry of the lacunary POM ligands. Moreover, achievement of the conditions allowing for self-assembly of multinuclear magnetic cores often leads to transformation / isomerization of the POT precursor itself. Nevertheless the screening approach has resulted in a number of POMs with SMM properties that are based on Mn^{III}, Co^{II} and Fe^{III} centers.

2.2.1. Mn^{III}-Based Species

The first successful use of the self-assembly approach for the preparation of POM-SMMs was achieved with Mn-containing polyanions. Like the species described in the previous section all of them contain Mn^{III} centers and are comprised of either a magnetic core based solely on manganese(III) ions or contain mixed-valent Mn^{II} / Mn^{III} or Mn^{II} / Mn^{III} / Mn^{IV} assemblies. This is undoubtedly related to the Jahn-Teller distortion of the Mn^{III} coordination geometry in its complexes leading to the appearance of an easy axis for magnetization and thus a magnetic anisotropy as the basis for a slow magnetization relaxation. The preparation of Mn^{III}-based POMs by a self-assembly processes utilizes partial or complete *in situ* oxidation of Mn^{II} centers by various oxidants or oxygen of air (in alkaline solutions) in the presence of POTs [22-33].

The first POMs incorporating a Mn^{III}-based magnetic core with SMM properties (and the first transition metal-incorporating POM-SMMs) were reported in 2008 by Cronin's group. The polyanions $[\{B\text{-}\alpha\text{-}XW_9O_{34}\}_2\{Mn^{III}_4Mn^{II}_2O_4(H_2O)_4\}]^{12-}$ (Mn_6-POM, X = Si, Ge) were synthesized by reaction of $[\gamma\text{-}XW_{10}O_{36}]^{8-}$ with $MnSO_4{\cdot}H_2O$ in aqueous medium containing morpholine (pH 7.2-7.9) and were isolated as hydrated morpholine (Ge) or mixed alkali metals/morpholine (Si) salts. During the reaction the dilacunary Keggin-type polyanions $[\gamma\text{-}XW_{10}O_{36}]^{8-}$ undergo a transformation into trilacunary species $\{B\text{-}\alpha\text{-}XW_9O_{34}\}^{10-}$ which sandwich the mixed-valent hexanuclear cationic $\{Mn^{III}_4Mn^{II}_2O_4(H_2O)_4\}^{8+}$ core. The magnetic $\{Mn^{III}_4Mn^{II}_2O_4(H_2O)_4\}$ assembly has a C_i-symmetric double-cubane structure where the two $\{Mn^{II}Mn^{III}_3O_4\}$ cubane subunits share two Mn^{III} centers (Fig. 2, top left). The four Jahn-Teller axes in the $\{Mn^{III}_4Mn^{II}_2O_4(H_2O)_4\}$ motif are thus aligned nearly parallel to each other. Interestingly, the difference of Ge–O and Si–O bonds in XW_9 POT units (1.733(3) Å *vs* 1.623(1) Å) causes some pronounced variations in the geometry of the $\{Mn^{III}_4Mn^{II}_2O_4(H_2O)_4\}$ cores in these two Mn_6-POMs. The magnetic core in the Ge derivative is thus contracted by 0.22 Å (with respect to the distance between two POT ligands) compared with the Si-based polyanion. This produces some differences in the magnetic behavior of these two polyanions despite the apparent similarity of their structures.

The analysis of the *dc* magnetic susceptibility measurements on Mn_6-POMs yielded competing ferromagnetic exchange interactions between the Mn^{II} and Mn^{III} centers ($J_{2\text{-}3}$ =

+6.5 cm^{-1} for Ge and +5.5 cm^{-1} for Si) and between the Mn^{III} centers through two μ_3-O groups with the Mn–O–Mn angle of about 90 ° ($J_{3\text{-}3}$ = +3.5 cm^{-1} for Ge and +4.5 cm^{-1} for Si) as well as strong antiferromagnetic exchange interactions between the Mn^{III} centers with the Mn–O–Mn angle of about 180 ° ($J'_{3\text{-}3}$ = –56.0 cm^{-1} for Ge and –59.5 cm^{-1} for Si) resulting in a ground state with the effective spin S = 5 for the both polyanions. The fitting of low-temperature (1.8 – 7.0 K) magnetization data at different fields confirmed the S = 5 ground state and yielded the following ZFS parameters: D = –0.67 cm^{-1}, g = 1.94 for the Ge derivative and D = –0.62 cm^{-1} and g = 1.99 for the Si-containing polyanion.

The *ac* susceptibility studies showed frequency-dependent behavior for $\chi'T$ *vs* T and appearance of a significant χ'' component below 5 K for the Ge derivative. The effective energy barrier U_{eff} was determined to be 10.3 cm^{-1} which is lower than the theoretically predicted barrier of 11.8 cm^{-1} obtained from the fitting of the $M(H/T)$ data. This indicates an important contribution of quantum tunneling relaxation pathways, apparently arising from the presence of transverse anisotropy due to C_i symmetry of the magnetic core in Mn_6-POMs. The pre-exponential factor τ_0 is equal to 3.1×10^{-7} s. No out-of-phase magnetic susceptibility was observed above 1.8 K for the Si analogue which most likely indicates a lower energy barrier for the magnetization reorientation in this case. Pulsed-field measurements on the Ge derivative at different sweep-rates at 1.6 and 0.5 K showed magnetization hysteresis with step-like features with 0.78 T peak separations, confirming quantum tunneling of the magnetization (QTM). The $|D|$ value of 0.71 cm^{-1} estimated from the field separation is in a good agreement with the value calculated from the fitting of the magnetization data (0.67 cm^{-1}) [25].

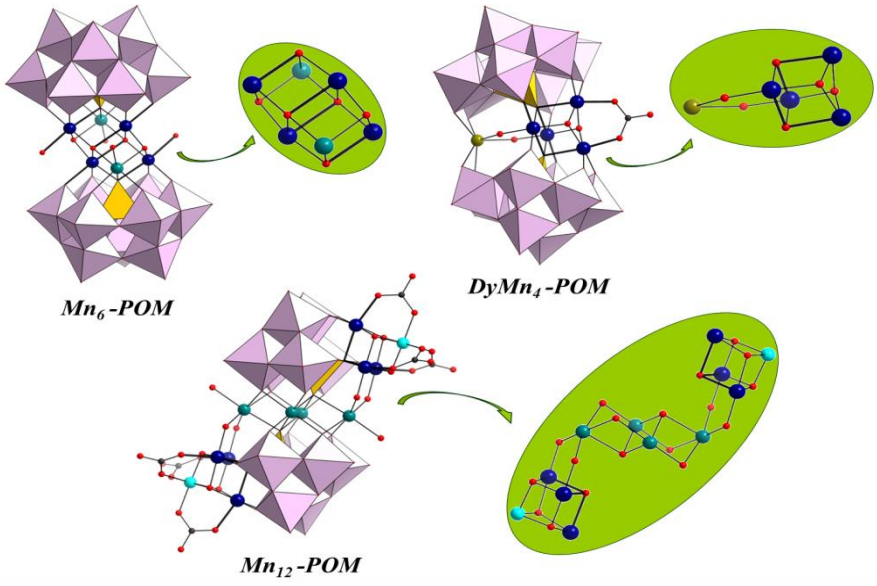

Figure 2. Structure of the Mn_6-POM (top left), $DyMn_4$-POM (top right) and Mn_{12}-POM (bottom) polyanions. Color legend as in Fig. 1. Mn^{II} are shown as blue-green spheres.

Reaction of Mn^{II} ions with $[\gamma\text{-}SiW_{10}O_{36}]^{8-}$ in water in the presence of morpholine combined with a gradual increase of the pH to 10 with K_2CO_3 solution led to polyanions $[\{KMn^{III}_4(\mu_3\text{-}O)_2(\mu_2\text{-}OH)_2(CO_3)\}(\beta\text{-}SiW_8O_{31})_2]^{15-}$ (KMn_4-POM) isolated as $K_9Na_6[KMn_4$-

POM]·22H_2O salt. The polyanions contain a {$Mn^{III}_4(\mu_3\text{-}O)_2(\mu_2\text{-}OH)_2$} cubane-like magnetic core stabilized by two {β-SiW_8O_{31}} POT units, a K^+ ion and a CO_3^{2-} group. The magnetic measurements indicated competitive antiferromagnetic and ferromagnetic interactions resulting in an $S = 4$ ground state. Fitting of the reduced magnetization data gave $D = -0.62$ cm^{-1} and $E = 3.5\times10^{-5}$ cm^{-1} values with $g = 1.94$. *AC* susceptibility measurements (at zero and 5 Oe *dc* fields) showed a frequency-dependent χ" signal below 2.5 K evident of slow relaxation of the magnetization. In this case the authors were not able to estimate the effective energy barrier for this compound due to the absence of the maxima on the χ" *vs T* plots [31].

It was also possible to isolate polyanions [{$Dy^{III}Mn^{III}_4(\mu_3\text{-}O)_2(\mu_2\text{-}OH)_2(H_2O)(CO_3)$}($\beta$-$SiW_8O_{31})_2$]$^{13-}$ ($DyMn_4$-POM) with structure similar to KMn_4-POM (Fig. 2, top right), where the K^+ ion is replaced by Dy^{III}, which were crystallized as the salt K_7Na_6[$DyMn_4$-POM]·21H_2O. The analysis of magnetic data for $DyMn_4$-POM using an empirical method implemented by Kahn [34] which takes into consideration the data for the KMn_4-POM; this suggested an antiferromagnetic coupling between the Mn^{III} and Dy^{III} ions in the {$Dy^{III}Mn^{III}_4O_4$} unit. As for KMn_4-POM, the reduced magnetization *vs H*/*T* measured for $DyMn_4$-POM exhibits weak separated isofield lines, but it was impossible to estimate the ZFS parameters due to the orbital contribution of the Dy^{III} ion. The *ac* susceptibility measurements (zero *dc* and 2 Oe *dc* fields) showed frequency-dependent signal below 4 K but no peak until 1.8 K [31]. The derivatives with other Ln^{III} centers [{$Ln^{III}Mn^{III}_4(\mu_3\text{-}O)_2(\mu_2\text{-}OH)_2(H_2O)(CO_3)$}($\beta$-$SiW_8O_{31})_2$]$^{13-}$ (Ln = Ho^{III}, Tm^{III}, Yb^{III}, Sm^{III}, Gd^{III}, Er^{III} and Ce^{IV}) have also been synthesized [33], however, as of now no magnetic studies on these species are available. It is also noteworthy that the structure of the MMn_4 core in KMn_4-POM and $DyMn_4$-POM intriguingly resembles that proposed for the Mn_4Ca OEC in PSII [35-36].

The similar approach, namely, reacting Mn^{II}, [β_2-$SiW_{11}O_{39}$]$^{8-}$ and 2,3-pyrazinedicarboxylic acid in H_2O with slow adjustment of the pH of the reaction mixture to 10.2 with K_2CO_3 solution, led to a polyanion comprising Mn ions in three oxidation states, [{$Mn^{IV}_2Mn^{III}_6Mn^{II}_4(\mu_3\text{-}O)_6(\mu\text{-}OH)_4(H_2O)_2(CO_3)_6$}{*B*-$\beta$-$SiW_6O_{26}$}$_2$]$^{18-}$ (Mn_{12}-POM). The polyanion consists of a belt of four Mn^{II} centers sandwiched between two {*B*-β-$SiW_6O_{26}Mn^{III}_3Mn^{IV}(\mu_3\text{-}O)_3(\mu\text{-}OH)_2(CO_3)_3$} subunits. The structure of the {$Mn^{III}_3Mn^{IV}(\mu_3\text{-}O)_3(\mu\text{-}OH)_2(CO_3)_3$} cubane-like motifs capping the SiW_6 fragments in these subunits is similar to that in $Mn_4P_2W_{15}$ with the bridging acetate groups replaced by carbonates. Overall, the magnetic core in Mn_{12}-POM polyanion comprises twelve Mn centers: four in the oxidation state +II, six in the oxidation state +III and two in the oxidation state +IV (Fig. 2, bottom).

The magnetic data on K_8Na_{10}[Mn_{12}-POM]·30H_2O are characteristic of dominant antiferromagnetic interactions within the Mn_{12} core. The susceptibility follows a Curie-Weiss expression ($C = 39.8$ cm^3Kmol^{-1}, $\theta = -33.5$ K) above 30 K and indicates significant thermal population of the low-lying excited states at 1.8 K which is similar to the behavior observed for Mn_4SiW_9-II discussed above [19]. Unfortunately it was impossible to estimate the ground spin state from the obtained data. The *ac* susceptibility measurements in a 1 Oe *ac* field oscillating at 30–10000 Hz showed an out-of-phase signal below 4 K that suggested SMM behavior of the complex, although no field-dependent magnetization hysteresis was detected at 1.8 K (using 100–200 Oe/min sweep rates). The corresponding effective energy barrier U_{eff} was estimated to be 14(1) cm^{-1} with $\tau_0 = 6(2)\times$ $\times10^{-10}$ s. At that, the relaxation times obey the Arrhenius law only above 2.3 K which, combined with the relatively small τ_0 value, may

implicate a fast quantum tunneling relaxation explaining the absence of a hysteresis loop on the *M vs H* curve [32].

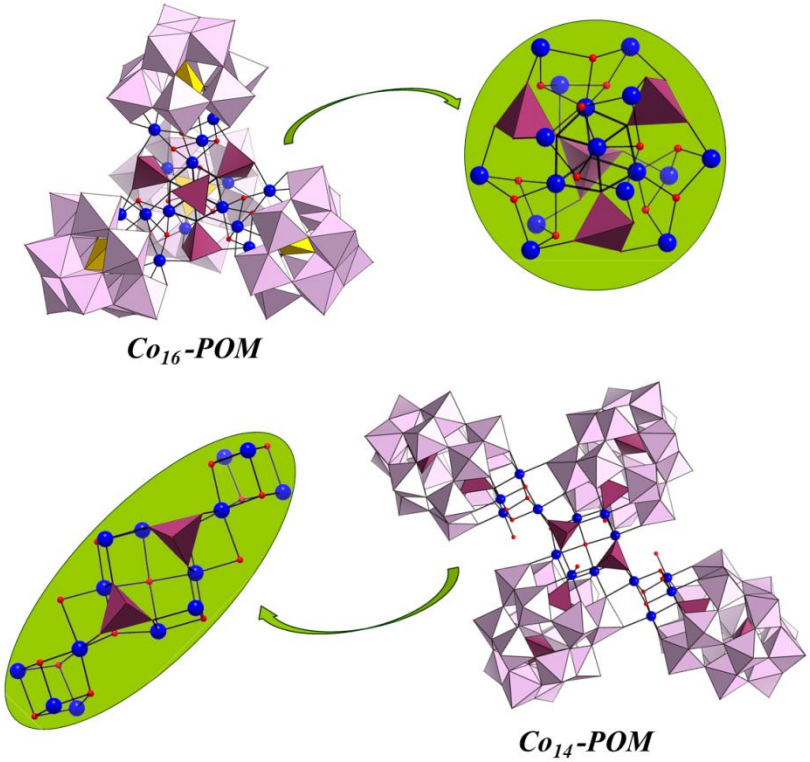

Figure 3. The structures of Co_{16}-POM (top) and Co_{14}-POM (bottom). Color legend: WO_6 pink octahedra, XO_4 yellow (X = P, Si, Ge) and PO_4 purple tetrahedra; Co^{II} blue, O red spheres. The magnetic cores of the POMs are enlarged and highlighted in the green insets, the bonds within the central $\{Co_4(OH)_4\}$ fragment of Co_{16}-core are emphasized in bold.

2.2.2. Co^{II}-Based Species

Another subclass of POM-SMMs based on multinuclear transition metal cores is constituted by Co^{II}-containing POTs. Co^{II} ions in POMs typically exhibit slightly distorted octahedral coordination geometries. Detailed effective model interpretation of magnetic data for Co^{II}-containing assemblies is often complicated due to prominent spin-orbit coupling contributions, in contrast to the Mn^{III}-based SMMs, where generally the contributions from the exchange interactions are significantly larger than the effects on the magnetic anisotropy [37]. To date all of the Co-POM-based SMMs are obtained by self-assembly processes starting from mononuclear Co^{II} precursors.

Kortz and Powell's group reported a series of polyanions $[\{Co_4(OH)_4PO_4\}_4(XW_9O_{34})_4]^{n-}$ (Co_{16}-POM, X = P^V, n = 28 [38]; X = Si^{IV}, Ge^{IV}, n = 32 [39]) incorporating a core composed of sixteen Co^{II} centers linked via hydroxo and phosphate groups, that is stabilized by four *A*-XW_9 trilacunary Keggin type POTs. The polyanions were prepared by reacting Co^{II} salts with the respective trilacunary POM $[A\text{-}\alpha\text{-}XW_9O_{34}]^{m-}$ and PO_4^{3-} in slightly basic aqueous media (pH ~ 8) and isolated as hydrated alkali metal salts. The polyanions Co_{16}-POM are comprised of four $\{Co_4XW_9\}$ units linked via four μ_3-OH^- and four μ_4-phosphate groups. Every

$\{Co_4XW_9\}$ building block is composed of the cubane-like $\{Co_4(OH)_3\}$ motif supported on the vacant site of *A*-XW_9 in a similar way to the Mn_4SiW_9 structure. Alternatively, the structure of the POM can be described as four Co_3XW_9 units connected to the central cubane-like $\{Co_4(OH)_4\}$ fragment by OH^- and PO_4^{3-} ligands (Fig. 3, top). The magnetic studies showed similar characteristics for all three polyanions, revealing only a small influence of the heterogroup nature on the magnetic properties in this case.

The *dc* susceptibility data and the field dependence of magnetization in the 2 – 5 K range suggest ferromagnetic interactions between the Co^{II} centers within the Co_{16} core indicating magnetic anisotropy as well as strong spin-orbit contribution in the Co^{II} ions. The dynamic measurements evidence SMM behavior for all three compounds. The relaxation time deduced from the frequency sweeping data in the temperature range 1.8 – 3.2 K for X = P and 1.8 – 2.8 K for X = Si, Ge follows an Arrhenius law and yield effective energy barrier values of 18.1 cm^{-1} (X = P), 17.2 cm^{-1} (X = Si) and 18.0 cm^{-1} (X = Ge) and pre-exponential factors τ_0 of 3.5×10^{-8} s (X = P), 1.6×10^{-8} s (X = Si) and 1.2×10^{-8} s (X = Ge); these are comparable with the values for the other reported Co^{II}-based SMMs [see for example 40-42]. The frequency dependence of the *ac* susceptibility in an applied *dc* field at 1.8 K indicated only a slight $\ln(1/\tau)$ shift with the increase of the *dc* field, showing an absence of pronounced quantum tunneling effects in these compounds that might be attributed to efficient separation or shielding of the magnetic cores by POT ligands [38-39].

Another example of a Co-POM SMM has been reported by Cronin's group. The polyanions $[\{Co_{14}O_8(OH)_7(HPO_4)_2(H_2O)_6\}(P_2W_{15}O_{56})_4]^{35-}$ (Co_{14}-POM) were synthesized using the similar strategy: namely, by reacting Co^{II} and trilacunary Wells-Dawson P_2W_{15} POTs in aqueous medium in the presence of PO_4^{3-} groups at pH 8.5, and isolated as the hydrated Li / Na salt $Li_{20}Na_{15}[Co_{14}\text{-POM}]\cdot110H_2O$. The polyanion possesses a cross-like structure which could be rationalized as the dimeric $\{(Co_3P_2W_{15}O_{56})_2(\mu_4\text{-O})\}$ motif with two $\{Co_4(\mu_3\text{-OH})_3P_2W_{15}O_{56}\}$ units connected on its opposite sides via μ_3-OH^- and μ_3-$PO_3(OH)^{2-}$ groups (Fig. 3, bottom). The structure of the each $\{Co_4(\mu_3\text{-OH})_3P_2W_{15}O_{56}\}$ building block represents a Co_4O_4 cubane motif supported on the vacant site of P_2W_{15} POT with an oxygen atom of its central PO_4^{3-} group acting as one of the Co_4O_4 cubane vertex in a way similar to the $Mn_4P_2W_{15}$ structure.

The temperature-dependent susceptibility data reported for the Co_{14}-POM are dominated by strong single-ion spin-orbit coupling effects that at higher temperatures cause significant deviations from the spin-only values for fourteen non-interacting Co^{II} centers. The *ac* measurements showed an appearance of an out-of-phase χ" magnetic susceptibility signal below 4 K indicating a slowing-down of the magnetization relaxation. The curves obtained in pulsed-field measurements at 1.6 K and 0.5 K exhibit hysteresis with only a weak dependence on sweep rate at 0.5 K. The hysteresis curve shows a steep increase up to approximately12 μ_B, and does not reach saturation at 30 T [43].

Heating of trilacunary Keggin-type polyoxotungstates $[A\text{-}\alpha\text{-}PW_9O_{34}]^{9-}$ with Co^{II} and alendronic acid ($(^+H_3N(CH_2)_3)(OH)C(PO_3H_2)_2$, H_5Ale) in aqueous medium at pH 7.5 resulted in another Co^{II}-based POM SMM $[\{(B\text{-}\alpha\text{-}PW_9O_{34})Co_3(OH)(H_2O)_2(Ale)_2\}_2Co]^{14-}$ (Co_7-POM) crystallized either as a hydrated mixed Na / NH_4^+ or a hydrated pure NH_4^+ salts. The Co_7-POM polyanion is comprised of two $\{B\text{-}\alpha\text{-}PW_9O_{34}Co_3\}$ subunits connected via an additional Co^{II} ion which also represents an inversion center of the polyanion. Two alendronate groups act as bridging ligands providing an additional connection between the central Co^{II} ion and

the Co_3 motif of the {*B*-*α*-$PW_9O_{34}Co_3$} units (Fig. 4). The χT *vs* T data indicated orbital momentum contributions and magnetic anisotropy typical for Co^{II} ions. Furthermore, the $\chi_M T$ data are consistent with ferromagnetic coupling within the Co_7 magnetic core, which could arise from magnetic interactions mediated via both hydroxo and bisphosphonate bridging ligands. The unambiguous determination of the ground state nature was not possible based on the obtained experimental data and could require some additional experiments (*e. g.* inelastic neutron scattering). Single-crystal field-dependent magnetization measurements at low temperature resulted in butterfly-shaped hysteresis loops at low temperatures, evident for a SMM behavior of the Co_7-POM with a blocking temperature of approximately 1 K. The small coercive field in the absence of an external magnetic field is again due to fast quantum tunneling relaxation mechanisms [44].

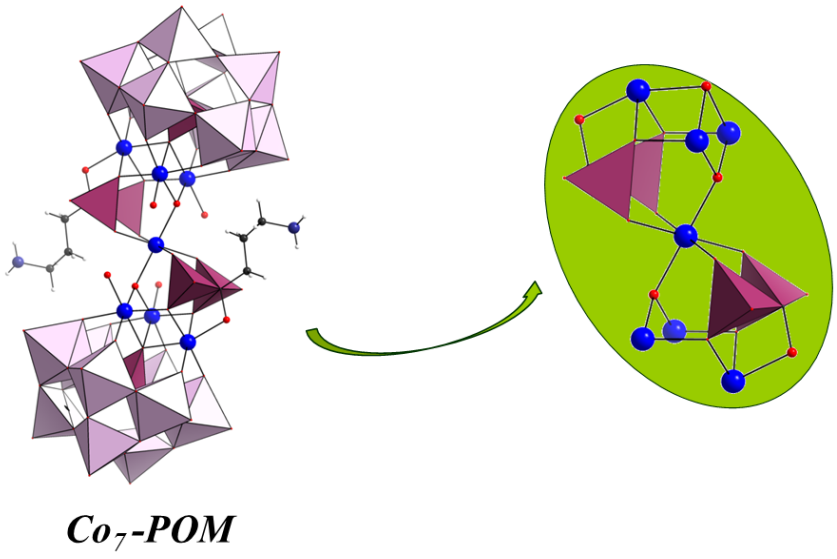

Figure 4. Structure of the M_7-POM (M = Co^{II}, Ni^{II}). Color legend: WO_6 pink octahedra, PO_4 purple tetrahedra; M blue, N violet, O red spheres. The magnetic core of the POM is enlarged and highlighted within the green inset.

2.2.3. Ni^{II}-based POM-SMM

A POM with a structure very similar to Co_7-POM, [{(*B*-*α*-PW_9O_{34})Ni_3(OH)$(H_2O)_2$(Ale)$_2$}$_2$Ni]$^{14-}$ (Ni_7-POM), has also been obtained by reacting Ni^{II} and alendronate with an excess of [*A*-*α*-PW_9O_{34}]$^{9-}$ at pH 7.5 in aqueous solution. The polyanion was isolated and characterized as both hydrated mixed Na^+ / K^+ and hydrated mixed Na^+ / NH_4^+ salts. The fitting of the χT *vs* T data yielded an S = 5 ground state which can be described by ferromagnetic interactions between the Ni^{II} ions within every {*B*-*α*-$PW_9O_{34}Ni_3$} unit (J_1 = +4.5 cm^{-1}, J_2 = +5.0 cm^{-1}) and weak antiferromagnetic interactions of the Ni^{II} centers of the {*B*-*α*-$PW_9O_{34}Ni_3$} unit with the central Ni^{II} ion (J_3 = –1.5 cm^{-1}, J_4 = 0 cm^{-1}; g = 2.27). The first excited state with S = 4 is separated from the ground state by only 1.0 cm^{-1}. Field-dependent single-crystal magnetization measurements at 0.5 K and variable field sweeping rates ranging from 0.008 to 0.280 Ts^{-1} resulted in butterfly-like hysteresis loops. Similar to Co_7-POM, the shape of the curves shows the absence of a significant

coercive field at zero external magnetic field. To date Ni_7-POM represents the only example of a POM-SMM based on Ni^{II} magnetic centers [45].

2.2.4. Fe^{III}-Based Species

Several POMs exhibiting slow magnetization relaxation incorporate multinuclear Fe^{III} assemblies. Interestingly, all of them are prepared by concurrent self-assembly of not only a magnetic core, but also of polyoxotungstate or polyoxomolybdate units that eventually stabilize the emergent core.

2.2.4.1. POM-SMMs Containing Only Fe^{III} Ions As Magnetic Centers

Mialane and co-workers reported on two Fe^{III}-POM SMMs possessing multi-iron magnetic cores where Fe^{III} ions exhibit either octahedral (in the following denoted as Fe^{III}_{oct}) or tetrahedral (Fe^{III}_{tet}) coordination geometry. Both species, $[\{(H_2O)(Fe^{III}_{oct})_3(Fe^{III}_{tet}W_9O_{34})\}_2(Fe_{tet}W_6O_{26})]^{19-}$ (Fe_9-POM) and $[Fe_4(H_2O)_2(FeW_9O_{34})_2]^{10-}$ (Fe_6 POM), have been prepared by hydrothermal reactions of Fe^{III}, WO_4^{2-} and tetramethylammonium in aqueous medium at pH 7 and isolated as hydrated mixed Na^+ / $[(CH_3)_4N]^+$ salts.

The Fe_9-POM contains two $\{(H_2O)(Fe^{III}_{oct})_3Fe^{III}_{tet}W_9O_{34}\}$ units, which could be considered as trilacunary $\{B\text{-}\alpha\text{-}Fe^{III}_{tet}W_9O_{34}\}$ Keggin-type POM coordinating three Fe^{III}_{oct} ions, and are connected via a central hexalacunary $\{Fe^{III}_{tet}W_6O_{26}\}$ fragment. The magnetic core in the Fe_9-POM is thus built of three tetrahedrally coordinated and six octahedrally coordinated Fe^{III} centers (Fig. 5, top left). The analysis of the field-/temperature-dependent magnetization curves for these species in the temperature range 2 – 8 K yields an $S = 15/2$ ground state with $g = 2.00$, $|D| = 0.24$ cm^{-1} and a rhombicity value $|E/D| = 0.18$. Analysis of the Fe–O distances and Fe–O–Fe angles in the Fe_9-POM allowed rationalizing the ground spin state in terms of antiferromagnetic interactions between the Fe^{III}_{oct} and Fe^{III}_{tet} and ferromagnetic coupling between the Fe^{III}_{oct} ions within the Fe_9 core. $M(H)$ studies on a single crystal show hysteresis loops at low temperature with the blocking temperature $T_b \sim 0.6$ K proving Fe_9-POM to be an SMM. The coercive field decreases with the increasing temperatures and increases with the increase of the sweep-field rate at a fixed temperature. The $M(H)$ curves do not show the step-like behavior characteristic of QTM and are typical for SMMs with a small magnetic anisotropy [46].

The Fe_6-POM consists of two trilacunary Keggin-type POTs $\{B\text{-}\alpha\text{-}Fe^{III}_{tet}W_9O_{34}\}$ sandwiching a tetranuclear $\{(H_2O)_2(Fe^{III}_{oct})_4O_{14}\}$ fragment (Fig. 5, top right). A fit of the magnetization curves resulted in the ground state with $S = 5$ and the anisotropy parameters $|D| = 0.49$ cm^{-1}, $|E/D| = 0$, $g = 2.00$. Single-crystal $M(H)$ studies yielded a hysteresis loop with steps at periodic values of the applied field ($T_b = 1.2$ K) that confirmed SMM behavior of Fe_6-POMs exhibiting QTM effects, which may be influenced by weak inter-cluster antiferromagnetic interactions. The field separation between the successive steps of 0.03 T yielded the experimental $|D|$ value of 0.47 cm^{-1} which is in good agreement with the data obtained by fitting $M(H/T)$ plots in the 2 – 4 K temperature range. The calculated effective energy barrier U_{eff} was 11.6 cm^{-1} with a pre-exponential factor τ_0 of 2.0×10^{-6} s [46].

It is also interesting to note that polyanion $[Fe^{II}_4(enH)_2(Fe^{III}W_9O_{34})_2]^{5-}$ with a very similar to Fe_6-POM structure and composition, containing four Fe^{II}_{oct} ions in the central belt position (instead of four Fe^{III}_{oct} in Fe_6-POM), exhibits no SMM properties but possesses a large magnetic anisotropy ($D = +1.12$ cm^{-1}) [47].

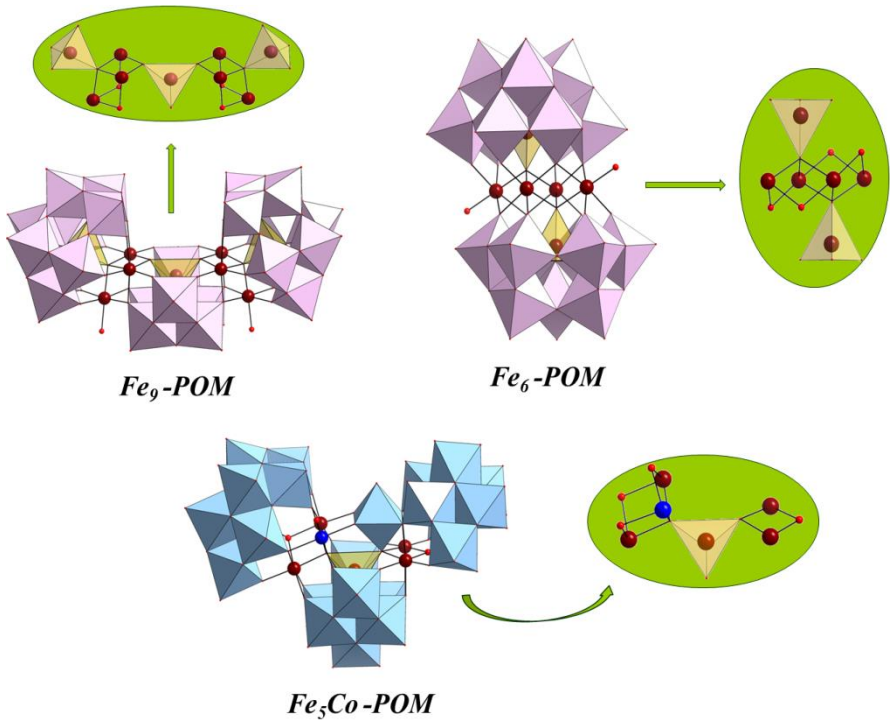

Figure 5. Structure of Fe^{III}-based POM-SMMs: Fe_9-POM (top left), Fe_6-POM (top right) and Fe_5Co-POM (bottom). Color legend: WO_6 pink and MO_6 blue octahedra, $Fe^{tet}O_4$ yellow tetrahedra; Fe brown, Co blue, O red balls. The magnetic cores of the POMs are enlarged and highlighted in the green insets.

The Fe_6-POMs were also grafted on a surface of single-wall carbon nanotubes (SWCNT) to explore whether the individual polyanions can still perform as SMMs when in contact with a conducting surface. The integrity of the polyanions absorbed on the SWCNT surface as well as the absence of the Fe_6-POM agglomeration have been confirmed by a number of analytical techniques including high-resolution transmission electronic microscopy, Raman spectroscopy, electrochemical measurements and others. The reduced magnetization (*M vs H*/*T*) plots (2 – 6 K) for the Fe_6-POM on SWCNT (Fe_6@CNT) are superimposable with those for the pure Fe_6-POM showing the retention of the magnetic anisotropy in the supported polyanions. Micro-SQUID measurements on Fe_6-POM powder and Fe_6@CNT also showed a hysteresis loop similar to the data obtained for the single crystals of Fe_6-POM providing evidence of the retention of a slow relaxation of the magnetization in these samples. The curves for the molecules isolated on SWCNT show a decrease of about 50 % of the remnant magnetization comparing with those of the powder Fe_6-POM sample, as well as the decrease of the coercive field from 3500 Oe for the powder to 900 Oe for Fe_6@CNT (0.04 K) which may be attributed to the absence of any interactions between the isolated Fe_6@CNT molecules which could still be present in the powder sample. The SMM behavior of the complexes was further supported by the dependence of the width of the hysteresis loop on the sweep rate of the applied magnetic field [48].

These results showcase that the rigid polyoxotungstate matrix can prevent any significant geometric deformations of the magnetic core due to interactions with surfaces which is often

the case for classical SMMs that are stabilized by semi-flexible organic ligands ([49]) and thus preserve the magnetic anisotropy behavior of the isolated molecules.

2.2.4.2. POM-SMMs Incorporating Both Fe^{III} and Co^{II} Magnetic Ions

The polyoxomolybdate $[Fe_5CoMo_{22}As_2O_{85}(H_2O)]^{15-}$ (Fe_5Co-POM) displays a *C*-shaped structure and incorporates both Co^{II} and Fe^{III} ions. The POM is built of a central $\{Fe^{III}_{tet}Mo_7O_{28}\}$ and two external $\{As^{III}Mo_7O_{27}\}$ structural units connected to each other via either $Fe^{III}_2Co^{II}$ or $Fe^{III}_2Mo^{VI}$ belts composed of corner-shared MO_6 octahedra (M = Fe, Co, Mo). All the centers within the magnetic Fe_5Co core are linked by oxo-ligands (Fig. 5, bottom). The POM was obtained by reacting ammonium heptamolybdate, $(NH_4)_6Mo_7O_{24}\cdot 4H_2O$, with $FeCl_3\cdot 6H_2O$ and $CoCl_2\cdot 6H_2O$ in a slightly acidic aqueous medium (pH ~ 6) and isolated as a hydrated ammonium salt. The *dc* susceptibility and field-dependent magnetization for this material are consistent with an $S = 11$ ground state produced by ferromagnetic coupling between the Fe^{III} ions combined with antiferromagnetic interactions between the Co^{II} and Fe^{III} centers. The *ac* susceptibility measurements showed frequency-dependent behavior and appearance of an out-of-phase signal χ'' at low temperatures. Fitting the temperature-dependent $\ln\tau$ data ($T = 0.5 - 1.8$ K) to the Arrhenius law yielded the values $U_{eff} = 6.05\ cm^{-1}$ and $\tau_0 = 6.33\times10^{-6}$ s. The plateau shape of the $\chi'_M T$ *vs* T plot above 4 K indicates a significant separation of the ground state from the excited states at low temperatures. The pulsed field measurement led to observation of a hysteresis with a butterfly shape at 0.5 K which disappears upon increasing the temperature to 1.8 K placing the blocking temperature within the range of 0.5 – 1.8 K [50].

3. Hybrid Assemblies Containing Cationic Transition Metal-Based Magnetic Units and POM Countercations

Another subclass of POM-SMMs is composed of a number of compounds where POMs have been used as bulky diamagnetic counterions to provide sufficient distance between positively charged magnetic clusters to prevent or at least minimize fast relaxation of magnetization via intermolecular coupling.

In these species POMs do not incorporate magnetic assemblies of transition metals in their structures but are linked with preformed magnetic units stabilized by inorganic moieties through weak electrostatic interactions, hydrogen bonds and in some cases also by covalent bonds between the magnetic metal centers and terminal, surface, oxygens of the polyanions. It should be noted, however, that even if these bonds have covalent character they are still much longer and weaker than the bonds which form between a heterometal center and oxygen atoms of a vacant site of a lacunary POM.

In some cases this approach indeed allowed the realization of intrinsic SMM properties of the magnetic species which were not pronounced in the absence of a diamagnetic dilution. In some other cases it was shown that the co-crystallization with POMs does not lead to any significant changes or improvements of the SMM performance though it does influence some magnetic characteristics. This allows for a fine-tuning of the magnetic properties of the SMM complexes. On the other hand, the composite materials composed of magnetic assemblies and the polyanions could serve as models for the deposition of magnetic clusters on metal oxide

surfaces to provide better understanding and control of the changes in the bond lengths and angles within the magnetic units which could be induced by such deposition.

3.1. Hybrid POM-SMM Salts Where Co-Crystallization of a SMM with POMs Resulted in Enhancement of Magnetic Relaxation Processes

The first experiments on preparation of the salts containing cationic SMM complexes and POMs as counterions were reported in 2003, when Coronado and co-workers studied the influence of co-crystallization of the Mn_{12}-SMM with various diamagnetic and paramagnetic polyanions on its magnetic properties. This required substitution of the acetate ligands in the charge-neutral Mn_{12}-OAc complex by (4-carboxybenzyl)tributylammonium groups leading to a positively charged magnetic $[Mn_{12}O_{12}(Z)_{16}(H_2O)_4]^{16+}$ species (Mn_{12}-Z, Z = $^{-}O_2C$-C_6H_4-$N(C_4H_9)_3$). This could then be isolated as salts with various anions formulated as $[Mn_{12}$-$Z](PF_6)_{16}$ (Mn_{12}-Z-PF_6), $[Mn_{12}$-$Z][W_6O_{19}]_8$ (Mn_{12}-Z-W_6), $[Mn_{12}$-$Z][PW_{12}O_{40}]_{16/3}$ (Mn_{12}-Z-PW_{12}), $[Mn_{12}$-$Z][(H_3O)NiPW_{11}O_{39}]_4$ (Mn_{12}-Z-$NiPW_{11}$) and $[Mn_{12}$-$Z][(H_3O)CoPW_{11}O_{39}]_4$ (Mn_{12}-Z-$CoPW_{11}$).

Table 1. The main magnetic characteristics of hybrid POM-SMM systems

Compound	*g*	*D*, cm^{-1}	H_c, G	H_{dc}, Oe	U_{eff}, cm^{-1}	τ_0, s	*Ref.*
Mn_{12}-Z-W_6	1.96	−0.40	750	0	35	5.7×10^{-9}	51
Mn_{12}-Z-PW_{12}	2.06	−0.40	460	0	35	6.0×10^{-9}	51
Mn_{12}-Z-$NiPW_{11}$	-	-	160	0	36	3.8×10^{-9}	51
Mn_{12}-Z-$CoPW_{11}$	-	-	75	0	37	1.7×10^{-9}	51
Mn_{12}-Z-PF_6	1.92	−0.44	3400	0	37	7.4×10^{-9}	51
Mn_4-Mo_6	-	−6.907	-	-	-	-	52
Mn_4-SiW_{12}	-	−6.614	-	-	-	-	52
Mn_4-ClO_4	-	−3.141	-	-	-	-	52
Mn_2-$AlMo_6$	1.98(2)	−0.69	-	700	9.2	7.2×10^{-7}	53
Mn_2-$CrMo_6$	1.92(2)	−0.90	-	600	6.3	16×10^{-7}	53
Mn_2-SW_{12}	2.066	−2.90	-	300	11.0	6.1×10^{-7}	54
				600	12.8	3.7×10^{-7}	54
				1000	13.7	3.2×10^{-7}	54
				1500	15.8	8.2×10^{-8}	54
Mn_2-SiW_{12}	2.091	−3.34	-	1000	10.7	4.1×10^{-7}	54
				1500	14.7	4.4×10^{-8}	54
Mn_2-Mn-SiW_{12}	-	-	-	500	10.2	3.8×10^{-7}	54
				1000	12.2	2.4×10^{-7}	54
				1500	14.6	6.4×10^{-8}	54
CuTb-IMo_6	-	-	-	0	11.9	4.0×10^{-6}	55
CuTb-$AlMo_6$	-	-	-	0	14.5	1.1×10^{-6}	55

DC susceptibility studies on the hybrid salts with diamagnetic polyanions ($[W_6O_{19}]^{2-}$ and $[PW_{12}O_{40}]^{3-}$) showed that their magnetic properties are very similar to those of Mn_{12}-OAc and Mn_{12}-Z. The fitting of the reduced magnetization as a function of H/T in a 2 – 5 K temperature and 0.5 – 5 T magnetic field range yielded ground states with S = 10 and ZFS parameters shown in Table 1. The *dc* data on the salts containing paramagnetic $[(H_3O)NiPW_{11}O_{39}]^{4-}$ and $[(H_3O)CoPW_{11}O_{39}]^{4-}$ showed a significant influence of the magnetic metals incorporated into POM species; however, it was impossible to accurately take into account their contribution, especially in the absence of the detailed structural information for these materials.

Magnetic hysteresis loops for all the Mn_{12}-Z-POM salts were obtained on non-oriented powder samples. In all the cases it was impossible to reach saturation in a 5 T field. Interestingly, the Mn_{12}-Z-$NiPW_{11}$ and Mn_{12}-Z-$CoPW_{11}$ salts have lower coercive fields than the Mn_{12}-Z-PW_{12} sample. The *ac* magnetic susceptibility measurements with zero *dc* field showed an out-of-phase signal for all the hybrid salts indicating that the Mn_{12}-Z fragment retains its SMM behavior independently of the counteranion. The χ''_M *vs* T plots for all the Mn_{12}-Z-POM hybrids exhibit two relaxation peaks: a shoulder in the 2 – 3 K temperature range and a sharp peak in the 4 – 7 K temperature interval. This is in contrast to Mn_{12}-Z-PF_6 for which only one maximum is present on the $\chi''(T)$ curves. The appearance of the second relaxation peak is not unusual for the Mn_{12}-carboxylate family of compounds and is typically attributed to the presence of Mn_{12} isomers with differently orientated Mn^{III} Jahn-Teller axes. The lower temperature relaxation peak is the most intense in the case of Mn_{12}-Z-MPW_{11} derivatives and especially for Mn_{12}-Z-$CoPW_{11}$, which is evidence of enhancement of the magnetic relaxation mediated by the presence of paramagnetic counteranions. The values of U_{eff} and τ_0 calculated for the relaxation peak in the 4 – 7 K temperature range are shown in Table 1. The lower τ_0 values for the Mn_{12}-Z-MPW_{11} species in comparison with that of the diamagnetic derivatives are also in agreement with faster magnetic relaxation in the presence of magnetic POM counterions [51].

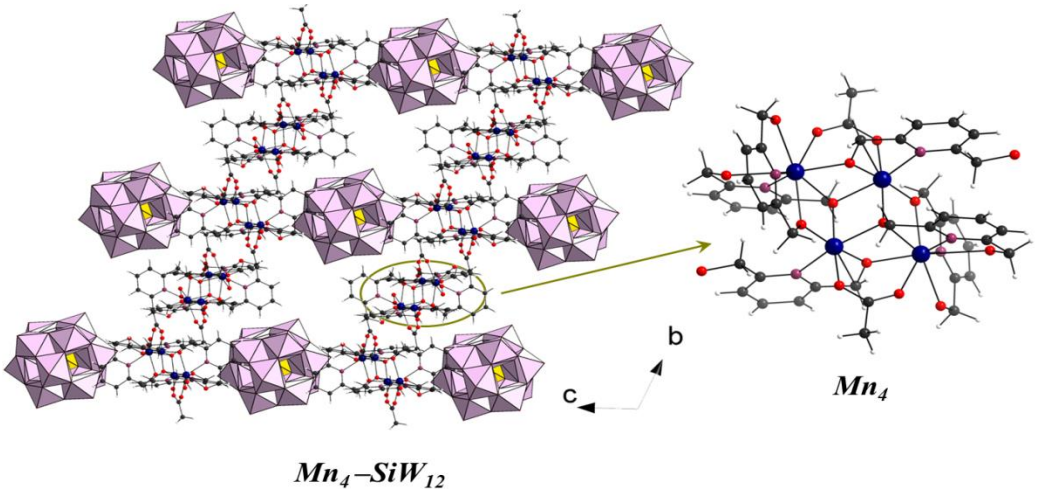

Figure 6. The structure of Mn_4-SiW_{12} (crystal packing shown along *a*) on the left and the Mn_4 complex on the right. Color legend: WO_6 pink octahedra, SiO_4 yellow tetrahedra; Mn blue, O red, C black, N pink, H white spheres.

Another SMM which was combined with various diamagnetic POMs acting as counter-ions is a tetranuclear complex $[Mn^{II}_2Mn^{III}_2(OAc)_2(\mu_2\text{-}C_7H_8NO_2)_6]^{2+}$ (Mn_4, $C_7H_8NO_2$ = deprotonated pyridine-2,6-dimethanol) possessing an S = 9 ground state and exhibiting superparamagnetic blocking below 2.5 K. The perchlorate salt of the complex $[Mn_4](ClO_4)_2$ (Mn_4-ClO_4) was reacted with a Lindquist-type polyoxomolybdate, $[Mo_6O_{19}]^{2-}$, and a Keggin-type POT, $[SiW_{12}O_{40}]^{4-}$, resulting in the $[Mn_4][Mo_6O_{19}]$ (Mn_4-Mo_6) and $[Mn_4]_2[SiW_{12}O_{40}]$ (Mn_4-SiW_{12}) hybrid salts. The crystal structures of the $[Mn_4](ClO_4)_2$ precursor and the two Mn_4-POM materials represent a layered networks composed of alternating cationic and anionic planes along the crystallographic *c* axis that are stacked on top of each other and held together by Coulomb interactions (Fig. 6). The Mn_4 units within each cationic layer are linked via π-π stacking interactions. The separation of the cationic layers depends on the nature of the counterion and increases by replacing ClO_4^- with polyanions as evidenced by a change of the crystallographic parameter *c* from 15.505 Å (Mn_4-ClO_4) to 15.854 Å (Mn_4-Mo_6) and 18.707 Å (Mn_4-SiW_{12}).

Fitting of the temperature-dependent susceptibility curves for the precursor and the two hybrid salts yielded positive coupling constants consistent with ferromagnetic coupling between the Mn^{II}–Mn^{III} (J_{23}) and Mn^{III}–Mn^{III} (J_{33}) centers and negative ZFS *D* parameters for the Mn^{III} ions. As such, the J_{23} and J_{33} values for the hybrid Mn_4-POM salts are much lower than those for the Mn_4-ClO_4 precursors.

This results in a much closer spacing of the energy levels in Mn_4-POM salts than in Mn_4-ClO_4 and thus in a smaller isolation of the S = 9 ground spin state. For example, in Mn_4-Mo_6 the spin state with S = 9 is separated from the S = 8 state by only a 1.6 cm^{-1} gap. This leads to lower effective molecular spin for the POM hybrid compounds than that observed for the perchlorate salt and subsequently should result in faster relaxation and lower blocking temperatures for the Mn_4-POM hybrids. The χ" curves obtained at zero *dc* field with the 3.95 G oscillating *ac* field for the Mn_4-POM salts did not have any maxima that would allow the straightforward calculation of the energy barriers U_{eff} and the τ_0 parameters for the Mn_4 units in these materials [52].

The enhancement of magnetic relaxation in the SMM-POM hybrids, despite the greater separation between the magnetic units of their layers in these compounds, observed in the studies discussed above may result from a high sensitivity of the spin levels distribution and magnetic characteristics of the polynuclear magnetic units to even very small changes in bond lengths and angles within the magnetic core.

This situation could be similar to that for the Mn_4SiW_9 polyanions (see part 1.1). This fact makes the co-crystallization approach for creating SMM or improvement / tuning their characteristics rather tricky and unpredictable. Nevertheless, the use of more rigid polydentate organic ligands, for example Schiff bases, for stabilization of magnetic units can help to reduce their geometric distortions due to co-crystallization with various anions. In the next subsection we provide several examples where a preparation of hybrid salts of positively charged magnetic units stabilized by Schiff base-type ligands with negatively charged POMs helped to reveal their intrinsic magnetic bistability characteristics.

3.2. Composite Salts Revealing Intrinsic SMM Properties of the Magnetic Units due to Co-Crystallization with POMs

The first success in enhancement of slow relaxation of magnetization of the magnetic units due to their co-crystallization with POMs was achieved with dimeric $\{Mn^{III}_2\}$ complexes stabilized by salen (N,N′-bis(salicylideneaminato)ethylene) ligands or their derivatives. These species can exhibit superparamagnetic behavior when the Jahn-Teller axes of their Mn^{III} centers are aligned in a common direction and a sufficient separation minimizing intermolecular exchange interactions is provided. Both of these criteria were met in the hybrid salts of $\{Mn^{III}_2\}$ salen units with Anderson-Evans-type POMs, $Na[Mn^{III}_2(salen)_2(H_2O)_2][XMo_6(OH)_6O_{18}]\cdot 20H_2O$ (Mn_2-XMo_6, X = Al^{III}, Gr^{III}) [53], and Keggin-type POMs, $[Mn^{III}_2(5\text{-MeOsaltmen})_2(acetone)_2][SW_{12}O_{40}]$ (Mn_2-SW_{12}), $[Mn^{III}_2(salen)_2(H_2O)_2]_2[SiW_{12}O_{40}]$ (Mn_2-SiW_{12}) and $[Mn^{III}_2(5\text{-Brsaltmen})_2][Mn^{III}(5\text{-Brsaltmen})(H_2O)(acetone)]_2[SW_{12}O_{40}]$ (Mn_2-Mn-SiW_{12}), where 5-Rsaltmen is N,N′-(1,1,2,2,-tetramethylethylene)-bis-(5-R-salicylideneaminate) and R is Br^- or MeO^- [54].

The structures of Mn_2-XMo_6 comprise $\{(H_2O)_2Na[XMo_6(OH)_6O_{18}]\}_n^{2n-}$ chains forming 2D anionic layers due to hydrogen bonds between the POM units and crystallization water molecules. The cationic $[Mn^{III}_2(salen)_2(H_2O)_2]^{2+}$ units in these structures are dispersed into the gaps between the anionic layers so that they all possess the same easy-axis direction, which is achieved by hydrogen bonding between the aqua ligands on the Mn^{III} centers and the O atoms of the XMo_6 polyanions. At the same time there are no π-π stacking interactions or direct hydrogen bonds between the adjacent $\{Mn^{III}_2\}$ complexes unlike in the structure of the $[Mn^{III}_2(salen)_2(H_2O)_2](ClO_4)_2$ precursor (Mn_4-ClO_4) [53].

The $\{Mn^{III}_2\}$ units and XW_{12} polyanions in Mn_2-SW_{12} and Mn_2-SiW_{12} form segregated columns along the crystallographical *a* axis, which are alternatingly arranged along the *b* and *c* axes (Fig. 7). Another salt containing Keggin-type polyanions, Mn_2-Mn-SiW_{12}, contains both dimeric $\{Mn^{III}_2\}$ aggregates and monomeric $\{Mn^{III}(5\text{-Brsaltmen})(H_2O)(acetone)\}$ complexes with the latter arranged into dimers via hydrogen bonds between the hydrogen atoms of the apical H_2O ligands and the phenoxy O atoms of the 5-Brsaltmen ligands. Here the $\{Mn^{III}_2\}$ units are directly connected to the SiW_{12} polyanions via weak covalent bonds between the Mn^{III} centers and terminal oxygens of the SiW_{12} polyanions to form infinite $\{[Mn^{III}_2(5\text{-Brsaltmen})_2][SiW_{12}O_{40}]\}_n^{2n-}$ chains which are aggregated into the anionic layers stacked along the *c* axis. The H-bonded $\{Mn^{III}(5\text{-Brsaltmen})(H_2O)(acetone)\}_2$-dimers are placed in the interspace between these layers [54]. The shortest intermolecular $Mn^{III}\ldots Mn^{III}$ distances in these polyanions are shown in Table 2.

Model fits to the temperature-dependent *dc* magnetic susceptibility and reduced magnetization as a function of H/T are in agreement with an $S = 4$ ground state for the $\{Mn^{III}_2\}$ units in the Mn_2-POM hybrid salts, which is also consistent with the positive sign of the simulated intradimer coupling constants J (Table 2). The estimated intermolecular exchange constants zJ' for Mn_2-XMo_6 and Mn_2-SW_{12} are about ten times lower than those for the Mn_2-ClO_4 precursor, evidencing the efficient suppression of interdimer magnetic exchange interactions via co-crystallization of the $\{Mn^{III}_2\}$ species and the POMs. At the same time the zJ' value is quite high for Mn_2-SiW_{12} which is most likely due to a shorter intermolecular $Mn^{III}\ldots Mn^{III}$ distances in this sample (Table 2) than in the other hybrid salts. The estimated magnetic ZFS parameters D for the Mn_2-XMo_6 and Mn_2-XW_{12} species (Table

1) are consistent with the SMM properties of the $\{Mn^{III}_2\}$ units in these composite salts although no magnetization hysteresis loops have been observed above 1.8 K for these materials.

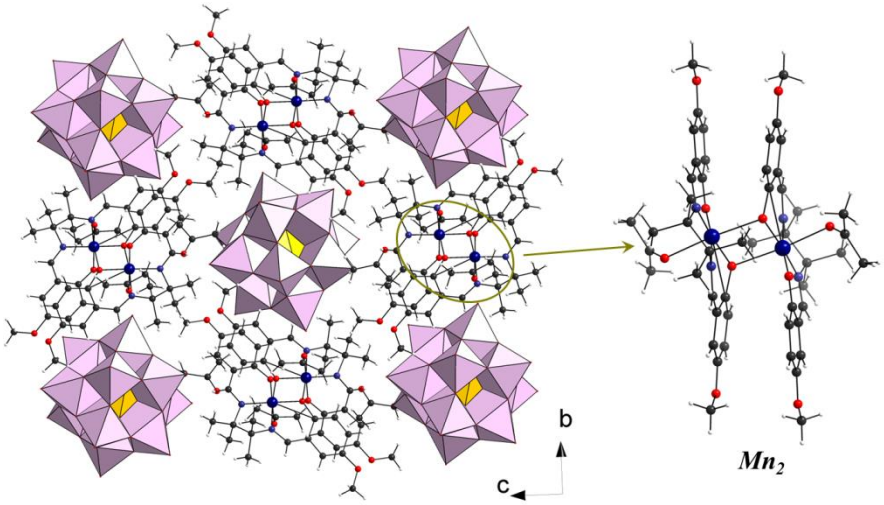

Figure 7. The structure of Mn_2-SW_{12} (crystal packing shown along the *a* axis) on the left and the Mn_2 complex on the right. Color legend is the same as in Fig. 6.

Table 2. The shortest intercluster distances in the Mn_2-based hybrid assemblies and the coupling constants between the Mn^{III} centers within the Mn_2 complex (*J*) and between the different Mn_2 species (*zJ'*)

Compound	Shortest Mn…Mn distance within the chain/ layer, Å	Shortest interchain / interlayer Mn…Mn distance, Å	J, cm^{-1}	zJ', cm^{-1}	*Ref.*
Mn_2-$AlMo_6$	8.49	15.38	+0.62(2)	−0.02(1)	53
Mn_2-$CrMo_6$	8.48	15.42	+0.44(2)	−0.03(1)	53
Mn_2-ClO_4	-	-	+1.47(5)	−0.18(1)	53
Mn_2-SW_{12}	9.74	13.37	+0.927(6)	0.011(1)	54
Mn_2-SiW_{12}	7.56	7.62	+0.68(1)	−0.595(4) ** −0.29 ***	54
Mn_2-Mn-SiW_{12}	14.61	11.317(8) 7.834(8)*	-	-	54

* Between monomers and dimers, respectively

** From fitting of $\chi T(T)$ data

*** From fitting of $M(H)$ data (g = 2.00)

The analysis of the *dc* data for the Mn_2-Mn-SiW_{12} salt is in agreement with ferromagnetic exchange interactions within the covalently bonded $\{Mn^{III}_2\}$-dimers and an antiferromagnetic coupling within the H-bonded $\{Mn^{III}\}_2$ units as well as with the presence of antiferromagnetic interdimer interactions between these units. However, the detailed analysis of magnetic data for this system was difficult due to its complexity.

The *ac* susceptibility measurements on the Mn_2-POM hybrid salts in the zero *dc* field showed only weak or even no out-of-phase χ" components which, however, become much

more pronounced if an external magnetic bias field is applied. Such behavior, on one hand, confirms SMM properties of the $\{Mn^{III}_2\}$ assemblies in the Mn_2-POM materials. On the other hand, it shows significant contribution of QTM effects which could be partially suppressed by application of a *dc* magnetic field (as discussed in the introduction). The exact energy barrier and τ_0 values calculated for Mn_2-POMs at different fields are shown in Table 1. It is worth noting that no χ" signal was observed for the Mn_2-ClO_4 sample, even in a non-zero bias field. For Mn_2-SiW_{12} the χ" *vs* ν (applied *ac* frequency) curves exhibit an anomalous field-independent peak at $\nu \leq 1$ Hz as well as an anomalous variation of χ"(*T*) for temperatures below 2.5 K. Such a field-independent peak could be attributed to the magnetically competing system, where the SMM character and long-range magnetic ordering are cooperative as a function of the *ac* frequency. This kind of behavior agrees with the large *zJ*' value produced by relatively short intermolecular Mn…Mn distances in the Mn_2-SiW_{12} sample, as well as with the presence of two differently oriented $\{Mn^{III}_2\}$ dimers in this structure, a feature which is not characteristic of the other Mn_2-XW_{12} or Mn_2-XMo_6 salts [53-54].

Another species which exposed its SMM properties by co-crystallization with POMs is a 3d-4f mixed-metal complex with the Schiff-base ligand N,N'-bis(3-methoxysalicylidene)ethylenediamine (denoted here as L), $\{Cu^{II}Tb^{III}L\}^{3+}$. While the precursor complex $[Cu^{II}Tb^{III}L(H_2O)_3Cl_2]Cl{\cdot}CH_3OH$ does not demonstrate superparamagnetic behavior, this is in contrast the case for the two hybrid salts of $\{Cu^{II}Tb^{III}L\}^{3+}$ with Anderson-Evans-type polyoxomolybdates, $[\{Cu^{II}Tb^{III}L(H_2O)_3\}_2\{IMo_6O_{24}\}]Cl{\cdot}2CH_3OH{\cdot}8H_2O$ (CuTb-IMo_6) and $[\{Cu^{II}Tb^{III}L(H_2O)_2\}_2\{AlMo_6O_{18}(OH)_6\}_2]{\cdot}CH_3OH{\cdot}10H_2O$ (CuTb-$AlMo_6$) [55].

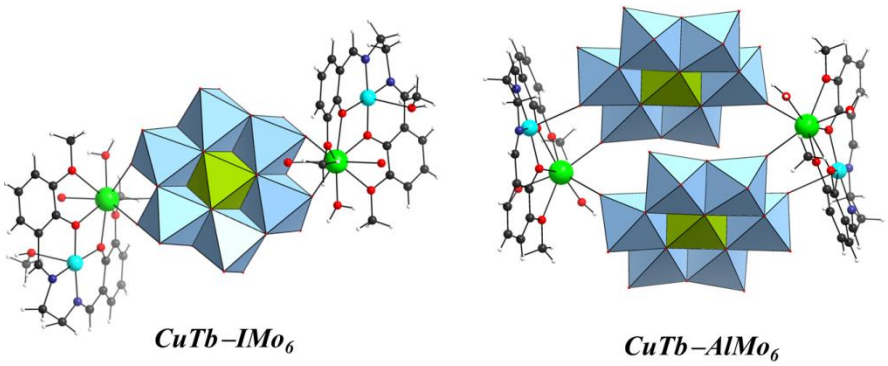

Figure 8. The structure of molecular units in CuTb-IMo_6 (left) and CuTb-$AlMo_6$ (right). Color legend: MoO_6 light blue and XO_6 (X = I, Al) green octahedra; Tb green, Cu cyan, C black, N blue, H white, O red spheres.

In CuTb-IMo_6 every $\{IMo_6\}$ species is coordinated by two $\{Cu^{II}Tb^{III}L(H_2O)_3\}^{3+}$ motifs supported on the opposite sides of the polyanion via two bonds between the Tb^{III} ions and terminal O atoms of $\{IMo_6\}$ (Fig. 8, left). Additionally, every Tb^{III} ion coordinates two phenolate and two ethoxy O atoms of the Schiff-base ligand L and three terminal aqua ligands and thus is nine-fold coordinated. The Cu^{II} ions in these species are five-fold coordinated with two imine N atoms and two phenolate O atoms of the Schiff-base ligands L and a terminal methoxy group. In CuTb-$AlMo_6$ the two cationic $\{Cu^{II}Tb^{III}L(H_2O)_2\}^{3+}$ units link two Anderson-Evans type polyanions $\{AlMo_6\}$ into a ring (Fig. 8, right). Each Cu^{II} ion in CuTb-$AlMo_6$ is five coordinated like in CuTb-IMo_6, however, its fifth coordination site is occupied

by an O atom of the $\{AlMo_6\}$ polyanion instead of a terminal methoxy group. The Tb^{III} ions in this compound possess the coordination number 8 and bind two O atoms of two different $AlMo_6$ units (one O atom from each polyanion), two phenolate and two ethoxy O atoms of the Schiff-base ligand L as well as two terminal water molecules. In the crystals of the both salts the magnetic 3d-4f assemblies are well separated and do not interact with each other, neither via π-π stacking nor via formation of hydrogen bonds. The other important feature of the CuTb-POM structures is coincident orientation of the Cu–Tb axes within the POM-suported $\{Cu^{II}Tb^{III}L\}^{3+}$ moieties. This contrasts the precursor $[Cu^{II}Tb^{III}L(H_2O)_3Cl_2]Cl{\cdot}CH_3OH$ where the $\{Cu^{II}Tb^{III}L\}^{3+}$ units are interlinked through strong hydrogen bonds and are arranged in two different orientations. It should also be mentioned that attachment of the $\{Cu^{II}Tb^{III}L\}^{3+}$ units onto POM surfaces changes the intercluster Cu…Tb distances and the dihedral $\{CuO_2Tb\}$ angle in comparison with the precursor salt.

The temperature-dependent *dc* susceptibility data on CuTb-XMo_6 could be explained in terms of the presence of weak ferromagnetic interactions between the Cu^{II} and Tb^{III} centers within the $\{Cu^{II}Tb^{III}L\}^{3+}$ moieties and the magnetic anisotropy of the Tb^{III} ion. The *ac* susceptibility measurements exhibit out-of-phase χ" signals below 10 K for both compounds. Interestingly, the relaxation times τ do not follow a simple Arrhenius law and become temperature-independent below 2.5 K as expected for SMMs in a pure quantum regime of relaxation. The characteristic time of QTM was found to be about 1.1×10^{-3} s. The energy gap U_{eff} and the pre-exponential factor τ_0 estimated from the thermally activated regime of relaxation are shown in Table 1. The obtained values of τ_0 are significantly larger than those of around 10^{-11} to 10^{-8} s usually expected for SMMs, and they are obviously enhanced by the presence of QTM. It also worth mentioning that the *ac* measurements on the precursor material did not reveal slow relaxation of the magnetization for this material [55].

In summary, the studies discussed in this subsection demonstrate that co-crystallization of magnetic complexes with POMs or the support of magnetic clusters on surfaces of polyoxoanions could indeed be a useful approach to reveal an intrinsic superparamagnetism of the multinuclear 3d or 3d-4f spin clusters. POM units in such hybrid salts play a double role, on one hand, providing sufficient separation between the magnetic units to prevent or at least minimize their interactions due to π-π stacking and/or hydrogen bonds; and, on the other hand allowing orientation of the easy axes of the magnetic units in a uniform direction.

CONCLUSION

Compared to an enormous array of polynuclear metal coordination complexes with organic ligands exhibiting SMM properties, the number of reported POMs showing slow relaxation of the magnetization is rather small and the subarea of POM-SMMs is still fairly young, having taken off only in 2008 [25].

In the species reported to date polyoxotungstates or -molybdates can in principle play two major roles. First, lacunary POT and POMo ligands can direct the assembly of the magnetic cores and simultaneously stabilize them within inorganic frameworks that are known to be thermally and redox robust. Second, plenary POTs of the Anderson-Evans, Keggin or Wells-Dawson structure type could be used as counteranions to provide sufficient separation between positively charged conventional magnetic complexes stabilized by organic ligands

and / or to induce uniform orientation of their molecular anisotropy axes within the resulting crystal lattices, and thus revealing the intrinsic magnetism in these magnetic species.

With respect to the first subclass of "genuine" POM-SMMs, the analysis of the available data allows suggestion of some major trends which could help to design a species with a better performance. It seems more preferable to use only inorganic POT or POMo ligands for stabilization of the magnetic core rather than both lacunary POMs and organic units. This can provide better shielding of the magnetic units to prevent or minimize quantum tunneling effects that derive from intermolecular magnetic interactions. In addition, it provides more rigidity to the magnetic core itself, diminishing the likelihood of significant distortions of the bond lengths and angles within the core producing significant variations of the magnetic properties as observed for some of the species discussed within this chapter. The overall stability of the polyanions containing only inorganic moieties also makes them attractive candidates for creating molecular spintronic devices, where magnetic molecules need to be sufficiently stable so as to not decompose when in contact with metallic electrode interfaces.

A separate very interesting direction in the area of POM-based nanomagnets is the development of lanthanide-functionalized POMs that represent prominent examples of single-ion magnets, which were not discussed within this chapter. Here the use of POMs could lead to unusual lanthanide ligand field symmetries, which in turn promises highly interesting magnetic phenomena.

To conclude, the area of POM-based SMMs has now lead to a critical mass of knowledge about the interrelations of structure and composition of magnetically functionalized polyanions in the context of SMM characteristics, as well as about the efficient synthetic pathways to POM-based SMMs. We expect that this will lead to an accelerated development of POM-based SMMs, which will likely unlock technological potential in, *e. g.*, molecular spintronics or quantum computing.

ACKNOWLEDGMENTS

Dr. Jan van Leusen, Dr. Jeffrey Rawson and Dr. Kirill Monakhov are gratefully acknowledged for proofreading the text and useful discussions.

REFERENCES

[1] Gatteschi, D.; Sessoli, R.; Villain, J. (2006). *Molecular Nanomagnets*. Oxford University Press, Oxford.

[2] van Leusen, J.; Speldrich, M.; Schilder, H.; Kögerler, P. (2014). Comprehensive Insight into Molecular Magnetism via CONDON: Full vs. Effective Models. *Coord. Chem. Rev.*, in press, DOI:10.1016/j.ccr.2014.10.011.

[3] Abragam, A.; Bleaney, B. (1970). *Electron Paramagnetic Resonance of Transition Ions*. Oxford University Press, Oxford.

[4] Griffith, J. S. (1971). *The Theory of Transition-Metal Ions*. Cambridge University Press, Cambridge.

[5] Bogani, L. (2015). Experiments on Molecular Magnets for Molecular Spintronics. *Structure and Bonding*, 164, 331–382. Springer International Publishing Switzerland.

[6] Clemente-Juan, J. M.; Coronado, E.; Gaita-Ariño, A. (2012). Magnetic polyoxometalates: from molecular magnetism to molecular spintronics and quantum computing. *Chem. Soc. Rev*. 41, 7464–7478

[7] Baldoví, J. J.; Coronado, E.; Gaita-Ariño, A.; Gamer, C.; Giménez-Marqués, M.; Mínguez Espallargas, G. (2014). SIM-MOF: Three-Dimensional Organisation of Single-Ion Magnets with Anion-Exchange Capabilities. *Chem. Eur. J*. 20, 10695 – 10702.

[8] Baldoví, J. J.; Clemente-Juan, J. M.; Coronado, E.; Duan, Y.; Gaita-Ariño, A.; Giménez-Saiz, C. (2014). Construction of a General Library for the Rational Design of Nanomagnets and Spin Qubits Based on Mononuclear f-Block Complexes. The Polyoxometalate Case. *Inorg. Chem*. 53, 9976–9980.

[9] Oms, O.; Dolbecq, A.; Mialane, P. (2012). Diversity in structures and properties of 3d-incorporating polyoxotungstates. *Chem. Soc. Rev*. 41, 7497–7536 and references therein.

[10] Zheng, S.-T.; Yang, G.-Y. (2012). Recent advances in paramagnetic-TM-substituted polyoxometalates (TM = Mn, Fe, Co, Ni, Cu). *Chem. Soc. Rev*. 41, 7623–7646 and references therein.

[11] Wu, Q.; Li, Y.-G.; Wang, Y.-H.; Wang, E.-B.; Zhang, Z.-M.; Clérac, R. (2009). Mixed-Valent $\{Mn_{14}\}$ Aggregate Encapsulated by the Inorganic Polyoxometalate Shell: $[Mn^{III}_{13}Mn^{II}O_{12}(PO_4)_4(PW_9O_{34})_4]^{31-}$. *Inorg. Chem*. 48, 1606-1612.

[12] Fang, X.; Speldrich, M.; Schilder, H.; Cao, R.; O'Halloran, K. P.; Hill, C. L.; Kögerler, P. (2010). Switching slow relaxation in a $Mn^{III}_3Mn^{IV}$ cluster: an example of grafting single-molecule magnets onto polyoxometalates. *Chem. Comm*. 46, 2760-62.

[13] Fang, X.; Luban, M. (2011). $\{Mn_{14}W_{48}\}$ aggregate: the perspective of isopolyanions as ligands. *Chem. Comm*. 47, 3066–3068.

[14] Fang, X.; Kögerler, P.; Furukawa, Y.; Speldrich, M.; Luban, M. (2011). Molecular Growth of a Core–Shell Polyoxometalate. *Angew. Chem. Int. Ed*. 50, 5212–16.

[15] Fang, X.; Kögerler, P.; Speldrich, M.; Schilder, H.; Luban, M. (2012). A polyoxometalate-based single-molecule magnet with an S=21/2 ground state. *Chem. Comm*. 48, 1218-1220.

[16] Fang, X.; McCallum, K.; Pratt, H. D.; Anderson, T. M.; Dennis, K.; Luban, M. (2012). A co-crystal of polyoxometalates exhibiting single-molecule magnet behavior: the structural origin of a large magnetic anisotropy. *Dalton Trans*. 41, 9867-9870.

[17] Huang, L.; Cheng, L.; Fang, W.-H.; Wang, S.-S.; Yang, G.-Y. (2013). Two Types of Polyoxometalates Based on Circular P_8W_{48} Cluster Units and Different Inclusions of Tetralanthanide and Octamanganese Centers. *Eur. J. Inorg. Chem*. 1693–98.

[18] Al-Oweini, R.; Bassil, B. S.; Palden, T.; Keita, B.; Lan, Y.; Powell, A. K.; Kortz, U. (2013). The Manganese(III)-Containing Tungstophosphate $[Mn^{III}_3(H_2O)_5(A\text{-}\alpha\text{-}PW_9O_{34})_2]^{9-}$. *Polyhedron* 52, 461-66.

[19] Al-Oweini, R.; Bassil, B. S.; Friedl, J.; Kottisch, V.; Ibrahim, M.; Asano, M.; Keita, B.; Novitchi, G.; Lan, Y.; Powell, A.; Stimming, U.; Kortz, U. (2014). Synthesis and Characterization of Multinuclear Manganese-Containing Tungstosilicates. *Inorg. Chem*. 53, 5663-5673.

[20] See for example Tuan, N. A., Sinh, N. H.; Chi, D. H. (2011). Tailoring magnetic properties in Mn_4 molecules: A way to develop single-molecule magnets. *J. Appl. Phys*. 109, 07B105 and references therein.

[21] Speldrich, M.; Schilder, H.; Lueken, H.; Kögerler, P. (2011). A Computational Framework for Magnetic Polyoxometalates and Molecular Spin Structures: CONDON 2.0. *Isr. J. Chem*. 51, 215-227.

[22] Zhang, X.-Y.; Jameson, G. B.; O'Connor, C. J.; Pope, M. T. (1996). High-Valent Manganese in Polyoxotungstates-II. Oxidation of the Tetramanganese Heteropolyanion $[Mn_4(H_2O)_2(PW_9O_{34})_2]^{10-}$. *Polyhedron* 15, 917-922.

[23] Zhang, X.-Y.; O'Connor, C. J.; Jameson, G. B.; Pope, M. T. (1996). High-Valent Manganese in Polyoxotungstates-3. Dimanganese Complexes of γ-Keggin Anions. *Inorg. Chem*. 35, 30-34.

[24] Rusu, D.; Rusu, M.; Patrut, A.; David, L. (2007). Physico-chemical characterization of the sandwich-type complexe of the trilacunary arseno(V)Polyoxotungstate with manganese (II). *Revista Chem*. 58, 484-88.

[25] Ritchie, C.; Ferguson, A.; Nojiri, H.; Miras, H. N.; Song, Y.-F.; Long, D.-L.; Burkholder, E.; Murrie, M.; Kögerler, P.; Brechin, E. K.; Cronin, L. (2008). Polyoxometalate-mediated self-assembly of single-molecule magnets: $\{[XW_9O_{34}]_2[(Mn^{III}_4Mn^{II}_2O_4(H_2O)_4]\}^{12-}$. *Angew. Chem. Int. Ed*. 47, 5609-5612.

[26] Dutta, D.; Jana, A. D.; Debnath, M.; Mostafa, G.; Clérac, R.; Tojal, J. G.; Ali, M. (2010). Design of Tri-Substituted Dodecatungstosilicate from a Trilacunary Silicotungstate by Insertion of Manganese Ions of $[Mn_3(\mu_3\text{-}O)(2\text{-}Cl\text{-}benzoato)_6(py)_3]$: Synthesis, Structure, Redox and Magnetic Studies. *Eur. J. Inorg. Chem*. 35, 5517-5522.

[27] Mitchell, S. G.; Miras, H. N.; Long, D.-L.; Cronin, L. (2010). A dimeric polyoxometalate sandwich motif containing a truncated $\{Mn_3O_4\}$ cubane core. *Inorg. Chim. Acta* 363, 4240–46.

[28] Mitchell, S. G.; Molina, P. I.; Khanra, S.; Miras, H. N.; Prescimone, A.; Cooper, G. J. T.; Winter, R. S.; Brechin, E. K.; Long, D.-L.; Cogdell, R. J.; Cronin, L. (2011). A Mixed-Valence Manganese Cubane Trapped by Inequivalent Trilacunary Polyoxometalate Ligands. *Angew. Chem. Int. Ed*. 50, 9154–57.

[29] Shevchenko, D.; Huang, P.; Bon, V. V.; Anderlund, M. F.; Kokozay, V. N.; Styring, S.; Thapper, A. (2013). Synthesis, crystal structure, mass spectrometry, electrochemistry and magnetism of a Mn^{III}-substituted trilacunary Keggin tungstosilicate. *Dalton Trans*. 42, 5130-39.

[30] Zhang, N.; Liu, B.; Liu, X.-M.; Ding, T.; Jia, Y.-Y.; Xue, G.-L. (2013). Triangular $\{Mn(OH)\}_3^{6+}$ fragment encapsulated in trivacant $[A\text{-}R\text{-}SiW_9O_{34}]^{10-}$ ligand. *Inorg. Chem. Commun*. 29, 30–32.

[31] Wu, H.-H.; Yao, S.; Zhang, Z.-M.; Li, Y.-G.; Song, Y.; Liu, Z.-J.; Han, X.-B.; Wang, E.-B. (2013). Heterometallic appended $\{MMn^{III}_4\}$ cubanes encapsulated by lacunary polytungstate ligands. *Dalton Trans*. 42, 342-46.

[32] Zhang, Z.-M.; Yao, S.; Li, Y.-G.; Wu, H.-H.; Wang, Y.-H.; Rouzières, M.; Clérac, R.; Su, Z.-M.; Wang, E.-B. (2013). A polyoxometalate-based single-molecule magnet with a mixed-valent $\{Mn^{IV}_2Mn^{III}_6Mn^{II}_4\}$ core. *Chem. Comm*. 49, 2515-17.

[33] Chen, Y.-Z.; Liu, Z.-J.; Zhang, Z.-M.; Zhou, H.-Y.; Zheng, X.-T.; Wang, E.-B. (2014). Systematic assembly of $\{LnMn^{III}_4\}$ appended cubanes with inorganic polyoxometalate ligands and their electrocatalytic property. *Inorg. Chem. Comm*. 46, 155–158.

[34] Kahn, M. L.; Mathoniere, C.; Kahn, O. (1999). Nature of the Interaction between Ln^{III} and Cu^{II} Ions in the Ladder-Type Compounds $\{Ln_2[Cu(opba)]_3\}\cdot S$ (Ln = Lanthanide Element; opba = ortho-Phenylenebis(oxamato), S = Solvent Molecules). *Inorg. Chem*. 38, 3692-97.

[35] Umena, Y.; Kawakami, K.; Shen, J.-R.; Kamiya, N. (2011). Crystal structure of oxygen-evolving photosystem II at a resolution of 1.9 Å. *Nature* 473, 55−60 and references therein.

[36] Pal, R.; Negre, C. F. A.; Vogt, L.; Pokhrel, R.; Ertem, M. Z.; Brudvig, G. W.; Batista, V. S. (2013). S_0-State Model of the Oxygen-Evolving Complex of Photosystem II. *Biochem*. 52, 7703 – 7706 and references therein.

[37] Murrie, M. (2010). Cobalt(II) single-molecule magnets. *Chem. Soc. Rev*. 39, 1986–1995.

[38] Ibrahim, M.; Lan, Y.; Bassil, B. S.; Xiang, Y.; Suchopar, A.; Powell, A. K.; Kortz, U. (2011). Hexadeca-Cobalt(II) Containing Polyoxometalate-Based Single-Molecule Magnet. *Angew. Chem. Int. Ed*. 50, 4708 –4711.

[39] Ibrahim, M.; Haider, A.; Lan, Y.; Bassil, B. S.; Carey, A. M.; Liu, R.; Zhang, G.; Keita, B.; Li, W.; Kostakis, G. E.; Powell, A. K.; Kortz, U. (2014). Multinuclear Cobalt(II)-Containing Heteropolytungstates: Structure, Magnetism, and Electrochemistry. *Inorg. Chem*. 53, 5179–5188.

[40] Zeng, M.-H.; Yao, M.-X.; Liang, H.; Zhang, W.-X.; Chen, X.-M. (2007). A Single-Molecule-Magnetic, Cubane-Based, Triangular Co_{12} Supercluster. *Angew. Chem. Int. Ed*. 46, 1832-35.

[41] Moubaraki, B.; Murray, K. S.; Hudson, T. A.; Robson, R. (2008). Tetranuclear and Octanuclear Cobalt(II) Citrate Cluster Single Molecule Magnets. *Eur. J. Inorg. Chem*. 4525-29.

[42] Galloway, K. W.; Schmidtman, M.; Sanchez-Benitez, J.; Kamenev, K. V.; Wernsdorfer, W.; Murrie, M. (2010). Slow magnetic relaxation in a 3D network of cobalt(II) citrate cubanes. *Dalton Trans*. 39, 4727-29.

[43] Lydon, C.; Sabi, M. M.; Symes, M. D.; Long, D.-L.; Murrie, M.; Yoshii, S.; Nojiri, H.; Cronin, L. (2012). Directed assembly of nanoscale Co(II)-substituted$\{Co_9[P_2W_{15}]_3\}$ and $\{Co_{14}[P_2W_{15}]_4\}$ polyoxometalates. Chem. Comm. 48, 9819-21.

[44] El Moll, H.; Dolbecq, A.; Marrot, J.; Rousseau, G.; Haouas, M.; Taulelle, F.; Rogez, G.; Wernsdorfer, W.; Keita, B.; Mialane, P. (2012). A Stable Hybrid Bisphosphonate Polyoxometalate Single-Molecule Magnet. *Chem. Eur. J*. 18, 3845-49.

[45] El Moll, H.; Rousseau, G.; Dolbecq, A.; Oms, O.; Marrot, J.; Haouas, M.; Taulelle, F.; Rivière, E.; Wernsdorfer, W.; Lachkar, D.; Lacôte, E.; Keita, B.; Mialane, P. (2013). Properties of a Tunable Multinuclear Nickel Polyoxotungstate Platform. *Chem. Eur. J*. 19, 6753-6765.

[46] Compain, J.-D.; Mialane, P.; Dolbecq, A.; Mbomekallé, I. M.; Marrot, J.; Sécheresse, F.; Rivière, E.; Rogez, G.; Wernsdorfer, W. (2009). Iron Polyoxometalate Single-Molecule Magnets. *Angew. Chem. Int. Ed*. 48, 3077-3081.

[47] Dolbecq, A.; Compain, J.-D.; Mialane, P.; Marrot, J.; Rivière, E.; Sécheresse, F. (2008). Water Substitution on Iron Centers: from 0D to 1D Sandwich Type Polyoxotungstates. *Inorg. Chem*. 47, 3371-78.

[48] Giusti, A.; Charron, G.; Mazerat, S.; Compain, J.-D.; Mialane, P.; Dolbecq, A.; Rivière, E.; Wernsdorfer, W.; Ngo Biboum, R.; Keita, B.; Nadjo, L.; Filoramo, A.; Bourgoin, J.-P.; Mallah, T. (2009). Magnetic Bistability of Individual Single-Molecule Magnets Grafted on Single-Wall Carbon Nanotubes. *Angew. Chem. Int. Ed*. 48, 4949-4952.

[49] See Cornia, A.; Mannini, M. (2015). Single-Molecule Magnets on Surfaces. *Structure and Bonding* 164, 293-330. Springer-Verlag Berlin Heidelberg and references therein.

[50] Zhen, Y.; Liu, B.; Li, L.; Wang, D.; Ma, Y.; Hu, H.; Gao, S.; Xue, G. (2013). Single-molecule magnet based on a C-type polyoxomolybdate with an S = 11 ground state: $[Fe_5CoMo_{22}As_2O_{85}(H_2O)]^{15-}$. *Dalton Trans*. 42, 58-62.

[51] Forment-Aliaga, A.; Coronado, E.; Feliz, M.; Gaita-Ariño, A.; Llusar, R., Romero, F. M. (2003). Cationic Mn_{12} single-molecule magnets and their polyoxometalate hybrid salts. *Inorg. Chem*. 42, 8019-27.

[52] Cardona-Serra, S.; Clemente-Juan, J. M.; Coronado, E.; Martí-Gastaldo, C.; Navarro-Moratalla, E. (2013). The Use of Polyoxometalates in the Design of Layer-Like Hybrid Salts Containing Cationic Mn_4 Single-Molecule Magnets. *Eur. J. Inorg. Chem*. 1903-09.

[53] Wu, Q.; Li, Y.-G.; Wang, Y.-H.; Clérac, R.; Lu, Y., Wang, E.-B. (2009). Polyoxometalate-based $\{Mn^{III}_2\}$-Schiff base composite materials exhibiting single-molecule magnet behavior. *Chem. Comm*. 5743-45.

[54] Sawada, Y.; Kosaka, W.; Hayashi, Y.; Miyasaka, H. (2012). Coulombic Aggregations of Mn^{III} salen-Type Complexes and Keggin-Type Polyoxometalates: Isolation of Mn_2 Single-Molecule Magnets. *Inorg. Chem*. 51, 4824-4832.

[55] Feng, X.; Zhou, W.; Li, Y.; Ke, H.; Tang, J.; Clérac, R.; Wang, Y.; Su, Z.; Wang, E.-B. (2012). Polyoxometalate-Supported 3d-4f Heterometallic Single-Molecule Magnets. *Inorg. Chem*. 51, 2722-24.